nature portfolio

https://doi.org/10.1038/s41586-025-08879-2

Supplementary information

Structurally complex phase engineering enables hydrogen-tolerant Al alloys

In the format provided by the authors and unedited

Supplementary Information for

Hydrogen-tolerant Al alloys via structurally complex phase engineering

Shengyu Jiang[1,+], Yuantao Xu[2,+,*], Ruihong Wang[3,+], Xinren Chen[4], Chaoshuai Guan[5], Yong Peng[5], Fuzhu Liu[1], Mingxu Wang[6], Xu Liu[7], Shaoyou Zhang[7], Genqi Tian[2], Shenbao Jin[7], Huiyuan Wang[7], Hiroyuki Toda[8], Xuejun Jin[2], Gang Liu[1,*], Baptiste Gault[4, 9,*], Jun Sun[1,*]

1. State Key Laboratory for Mechanical Behavior of Materials, Xi'an Jiaotong University, Xi'an 710049, China

2. Shanghai Key Laboratory of Materials Laser Processing and Modification, Shanghai Jiao Tong University, Shanghai 200240, China

3. School of Materials Science and Engineering, Xi'an University of Technology, Xi'an 710048, China

4. Max-Planck Institute for Sustainable Materials, Max-Planck-Str. 1, Düsseldorf 40237, Germany

5. School of Materials and Energy, Electron Microscopy Centre of Lanzhou University, Lanzhou University, Lanzhou 730000, China

6. School of Mechanical, electrical & Information Engineering, Shandong University, Weihai 264209, China

7. State Key Laboratory of High Performance Roll Materials and Composite Forming, School of Material Science and Engineering, Hebei University of Technology, Tianjin, 300130 China

8. Department of Mechanical Engineering, Kyushu University, Fukuoka 819-0395, Japan

9. Department of Materials, Imperial College, South Kensington, London SW7 2AZ, United Kingdom

+: These authors contribute equally to the paper.

*: Corresponding authors: xuyuantao@sjtu.edu.cn (YX); lgsammer@xjtu.edu.cn (GL); b.gault@mpie.de (BG); junsun@xjtu.edu.cn (JS)

Content

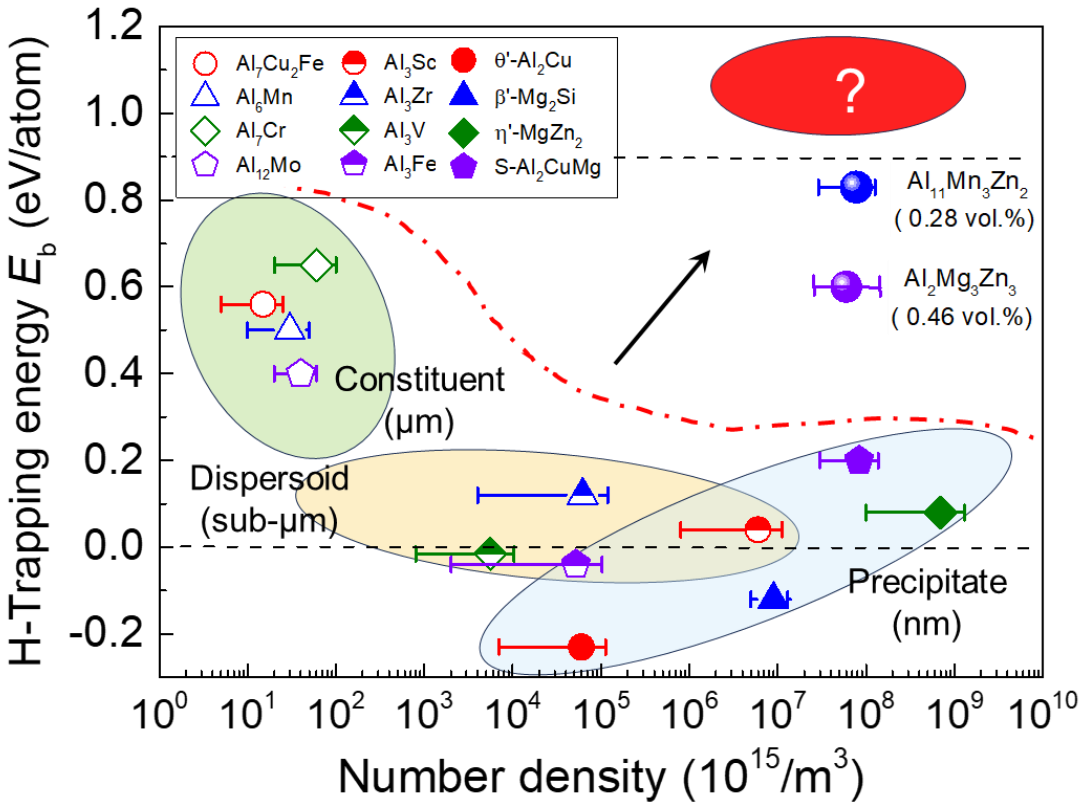

Supplementary Figure 1 | Intermetallic compound particles (ICPs) in Al alloys: trade-off relationship between H-trapping energy (E_b) and number density, two requisites for mitigating HE resistance. The ICPs that are predicted to have a high E_b normally exists as coarse constituent particles, in μm-scaled size and a low number density typically < 10^{18}/m^3. The IPCs that could be precipitated as high-density, nanosized precipitates (> 10^{20}/m^3) normally have a low E_b. The sub-μm-sized dispersoids generally exhibit a low number density and a low E_b. The exceptions are the newly-found $Al_{11}Mn_3Zn_2$ [S1] and $Al_2Mg_3Zn_3$ [S2] that show a high E_b and a high number density, but in a low volume fraction of only ~ 0.28 vol.% and ~ 0.46 vol.%, respectively. Novel ICPs with an extraordinary E_b (in particular > 0.9 eV/atom), a high number density (the same level as traditional precipitates), and simultaneously a great volume fraction (up to ~ 1.0 vol.%) (upright region highlighted in red) are urgently required for advanced HE-resistant Al alloys. The values of E_b are taken from ref.[S1], and the number density is estimated from refs.[S3-S13] (Al_7Cu_2Fe[S3], Al_7Cr[S4], Al_6Mn[S5], $Al_{12}Mo$[S6], β′-Mg_2Si[S7], η′-$MgZn_2$[S8], S-Al_2CuMg[S9], Al_3Zr[S10], Al_3V and Al_3Fe[S11], Al_3Sc[S12], θ′-Al_2Cu[S13]). The error bars represent the maximum and minimum values respectively.

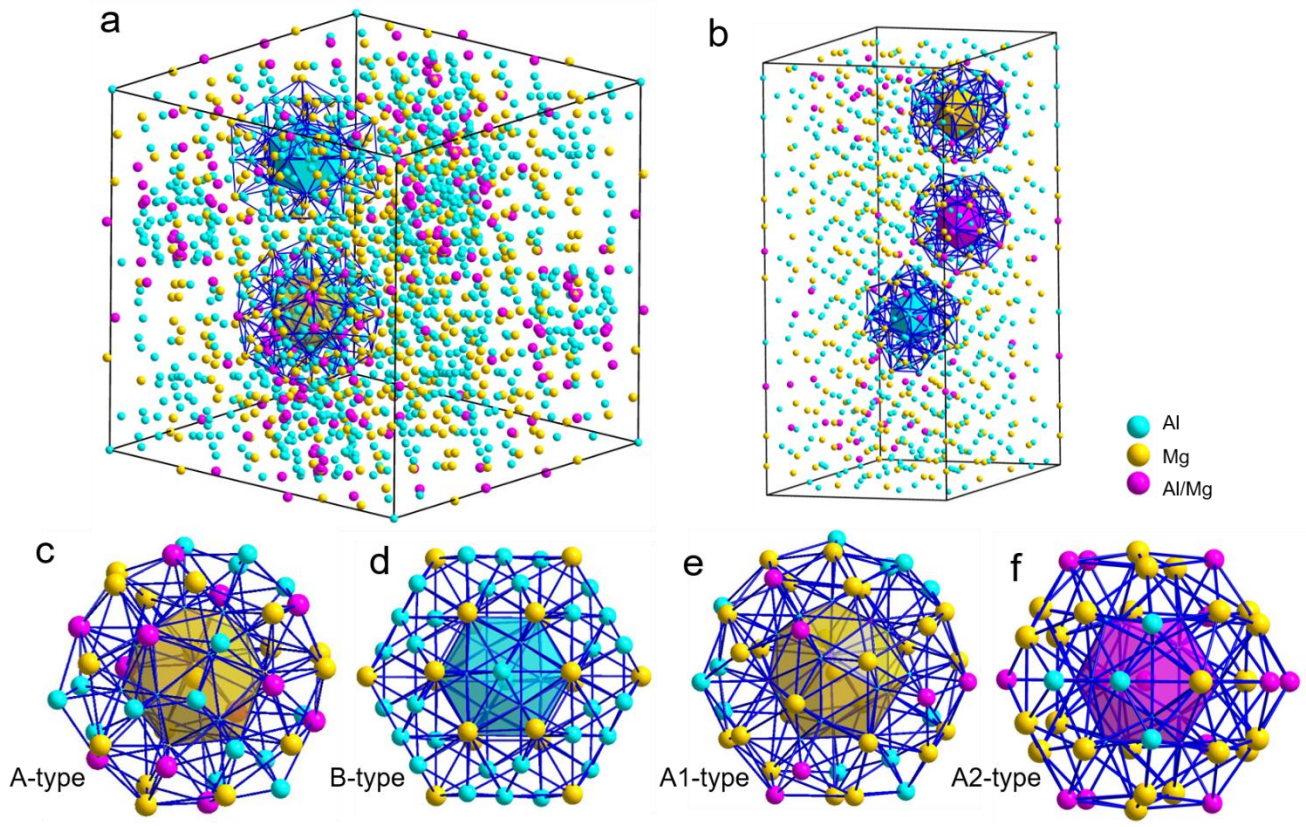

Supplementary Figure 2 | Crystal structure of the complex metallic phase Al_3Mg_2: cubic Samson-β-Al_3Mg_2 (a) and rhombohedral β′-Al_3Mg_2 (b), both with giant unit cells. In the nanocluster model[S14], the cubic β-Al_3Mg_2 is topologically described as an assembly of two types of two-shell nanoclusters, *i.e.*, A-type (c) and B-type (d). The rhombohedral β′-Al_3Mg_2 is topologically described as an assembly of B-type (d), A1-type (e), and A2-type (f) nanoclusters. The nanoclusters are typically indicated in (a) and (b), respectively.

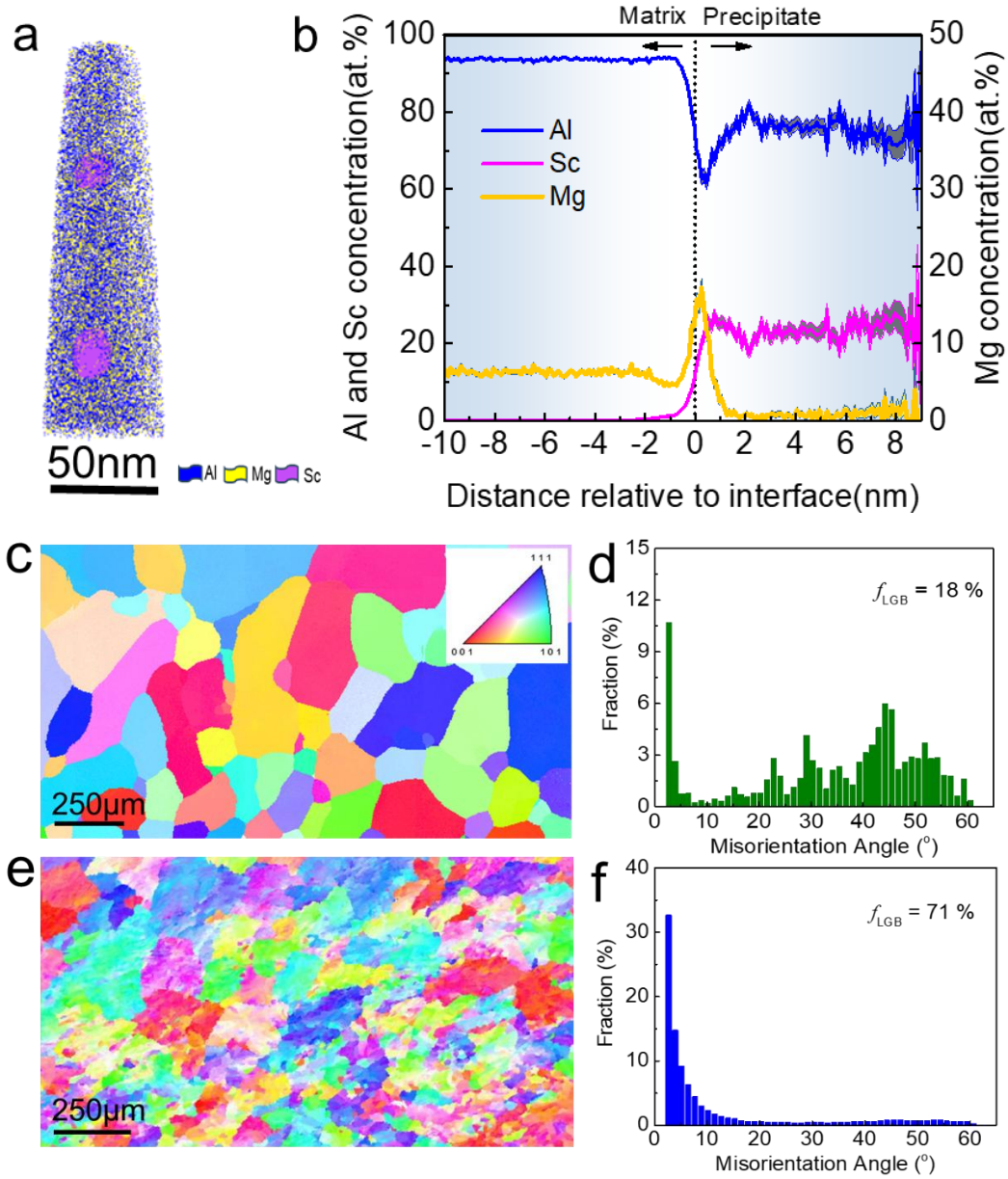

Supplementary Figure 3 | Microstructures of the Al-Mg-Sc-I vs. Al-Mg-I alloys. APT results (a) and composition proxigram cross the Al_3Sc/matrix interface (b) reveal a strong interfacial Mg segregation, with a high concentration up to > 15 at.%, in the Al-Mg-Sc-I alloy. Electron Back Scatter Diffraction (EBSD) images of the Al-Mg-I (c) and Al-Mg-Sc-I (e) alloys. The corresponding statistical results in (d) and (f) quantitatively show the percentage of low-angle grain boundaries (f_{LGB}) is only ~ 18% in the as-prepared Al-Mg alloy while up to ~ 71% in the as-prepared Al-Mg-Sc alloy.

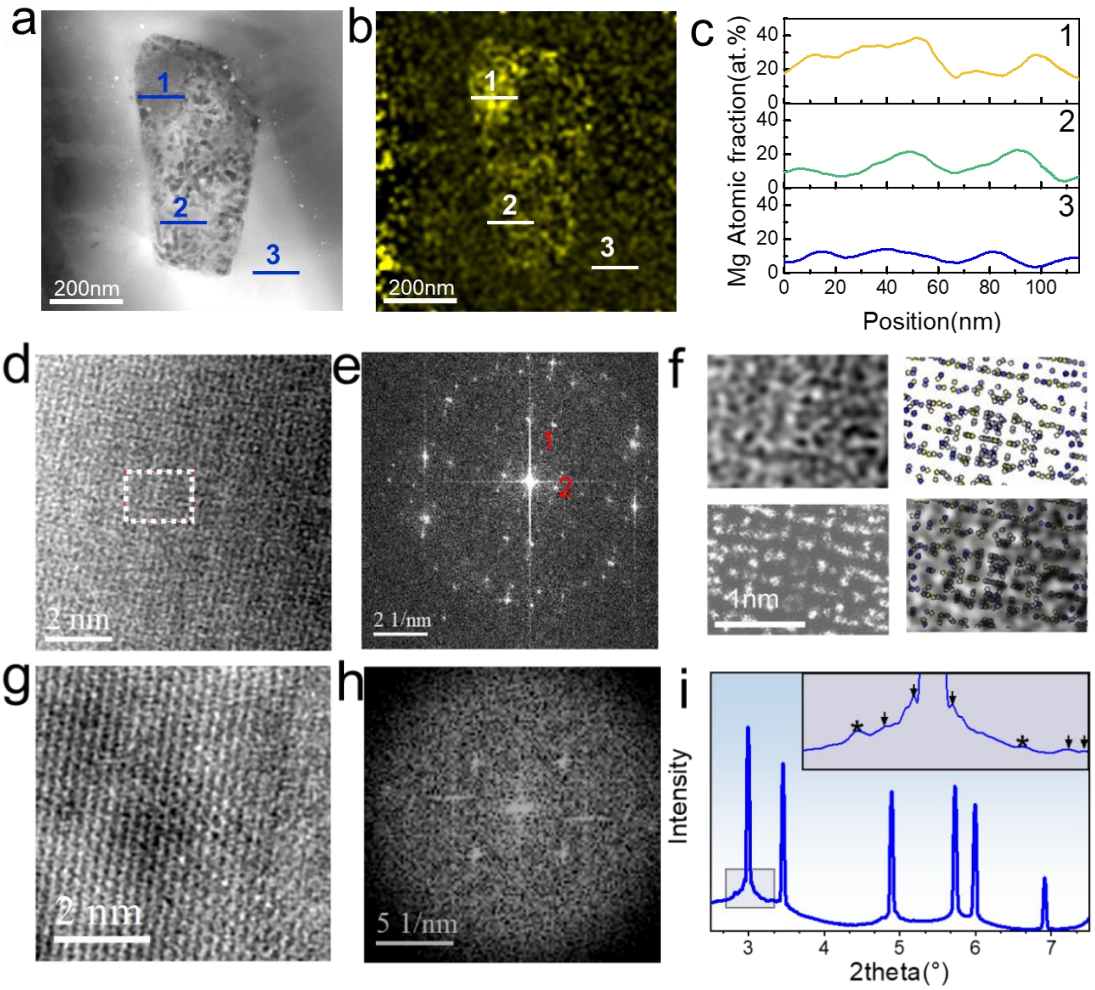

Supplementary Figure 4 | Complex metallic phase Al_3Mg_2 in the Al-Mg-II alloy. A representative HAADF-STEM image (a) and corresponding energy dispersive X-ray (EDX) Mg mapping (b) of a coarse intragranular Al_3Mg_2 particle in the Al-Mg-II alloy. (c) shows line scan of the Mg concentration according to lines #1, #2, and #3 marked in (a) and (b). Line #3 refers to the matrix adjacent to the Al_3Mg_2 particle. Representative HAADF-STEM image (d) and FFT image (e) corresponding to the region marked by line #1. Magnified image corresponding to the box region indicated in (d) is given in (f), in comparison with simulation result, crystal structure sketch, and overlapped image, to index the cubic β-Al_3Mg_2 structure. In (e), 1 and 2 represent $(1\bar{1}\bar{1})$ and (220), respectively, along the zone axis $[1\bar{1}2]$. HAADF-STEM image in (g) and FFT image (h) correspond to the region marked by line #2. The signal of Al_3Mg_2 structure is weak in (h), which is in agreement with the Mg-poor feature revealed by EDX. Overall, synchrotron X-ray diffraction results of bulk Al-Mg-II alloy display the peaks of both β-Al_3Mg_2 and β′-Al_3Mg_2 structure (i), where asterisks indicate the cubic β-Al_3Mg_2 peaks and arrows indicate the rhombohedral β′-Al_3Mg_2 peaks, see the summary in Supplementary Table 1. Note the region with a Mg concentration up to 40 at.% (b and c, marked by line #1)

has a stoichiometric composition of cubic-structured Samson-Al_3Mg_2, and the crystal structure was experimentally verified by high-angle annular dark-field scanning-transmission-electron microscopy (HAADF-STEM) as well as by synchrotron X-ray diffraction. While the region with a Mg concentration of ~ 25 at.% (marked by line #2) is characterized to be quasi β′-Al_3Mg_2 phase with a rhombohedral structure (g and h). Note that the phase transformation from metastable β′-Al_3Mg_2 phase to equilibrium β-Al_3Mg_2 phase happens around 210 °C. Although, we selected 250 °C for the second-step heat treatment in order to obtain full β-Al_3Mg_2 phase, the sluggish atomic diffusion in the CMPs limited the β′-Al_3Mg_2-to-β-Al_3Mg_2 transformation kinetics and the two phases coexist in the final material.

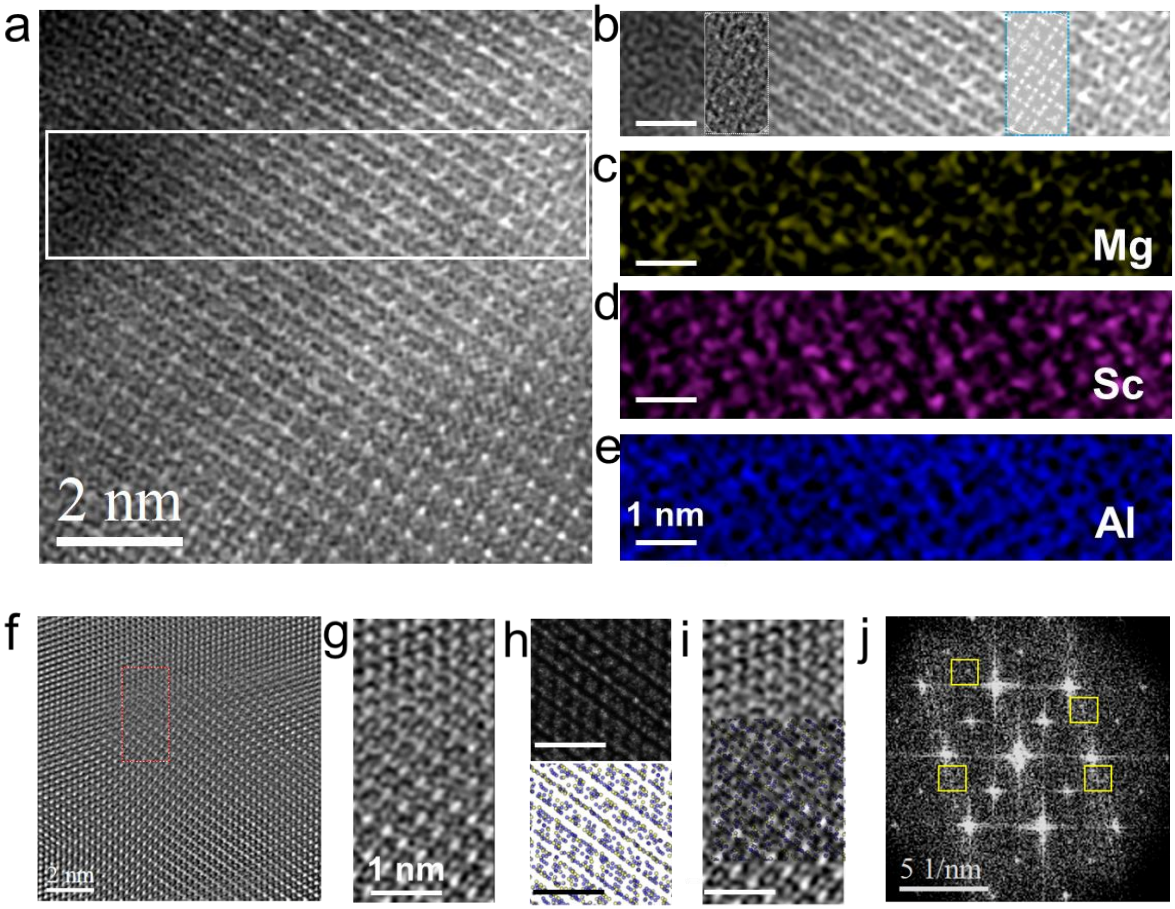

Supplementary Figure 5 | Complex metallic phase $Al_3(Mg, Sc)_2$ in the Al-Mg-Sc-II alloy. (a) A representative HAADF-STEM image to show Samson- $Al_3(Mg, Sc)_2$ nanophase in the Al-Mg-Sc-II alloy. (b) Local HAADF-STEM image corresponding to the region marked by white rectangle in (a). Coexistence of cubic β-$Al_3(Mg, Sc)_2$ phase (left part) and β′-$Al_3(Mg, Sc)_2$ phase (right part) is evident. Inserts in (b) are HAADF-STEM simulation images viewed along $[121]_{\beta}$ and $[\bar{1}\bar{3}4\bar{1}]_{\beta'}$, respectively, corresponding to the two phases. Elemental atomic mapping of Mg, Sc, and Al is present in (c), (d), and (e), respectively. (f) A representative HAADF-STEM image to show the Samson-$Al_3(Mg, Sc)_2$ phase (bottom part) formed on Al_3Sc nanoprecipitate (top part) in Al-Mg-Sc-II alloy, viewed along $\sim[31\bar{4}0]_{\beta'}$. (g) Magnified HAADF-STEM image corresponding to the region marked by a rectangle, in comparison with the HAADF simulation image (top in (h)) and crystal structure sketch of β′-$Al_3(Mg, Sc)_2$ phase (bottom in (h)). (i) The experimental image coincides well with the simulation image and crystal structure sketch by overlapping together. (j) FFT image indicates the coexistence of β′-$Al_3(Mg, Sc)_2$ and Al_3Sc phases.

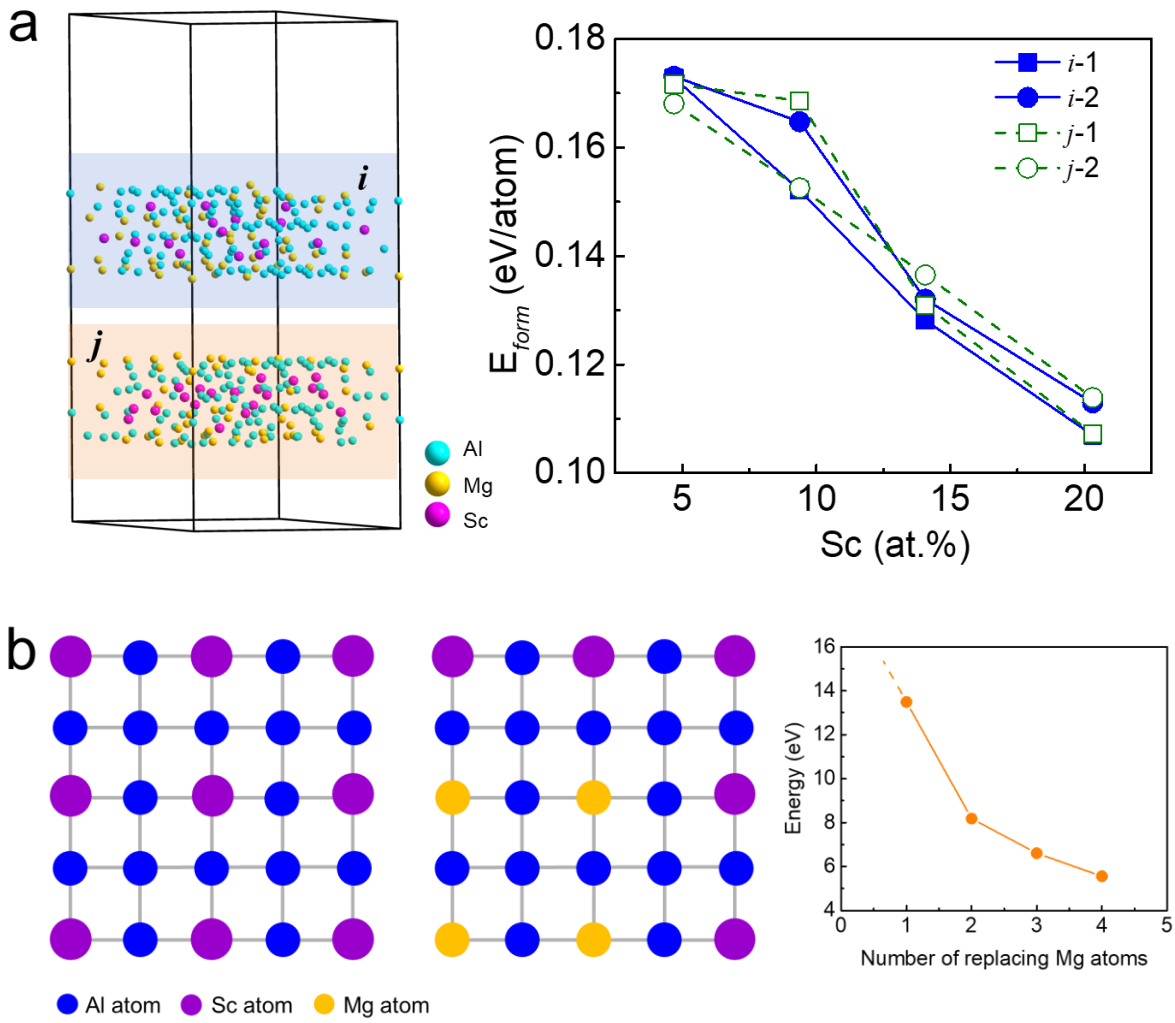

Supplementary Figure 6 | Simulations on the energy change by partial substitution. (a) DFT simulation results show the system energy is reduced (indicative of more stable condition) as the Mg positions in β′-Al_3Mg_2 phase are partially replaced by Sc atoms. Left is the slab model for simulation, where two typical layers of *i* and *j*, containing 101 Al atoms and 64 Mg atoms as the same, are respectively used by Sc partially replacing Mg. Since the Sc replacing are random, several simulations were performed for each layer to ensure the repeatability. Typical calculation results shown in right for comparison, *i.e.*, two for *i* (*i*-1 and *i*-2) and two for *j* (*j*-1 and *j*-2), verify the repeatability. (b) DFT calculations to show that the Mg intake into the Al_3Sc nanoprecipitates, by partially replacing Sc atoms, will reduce the energy and lead to a more stable condition.

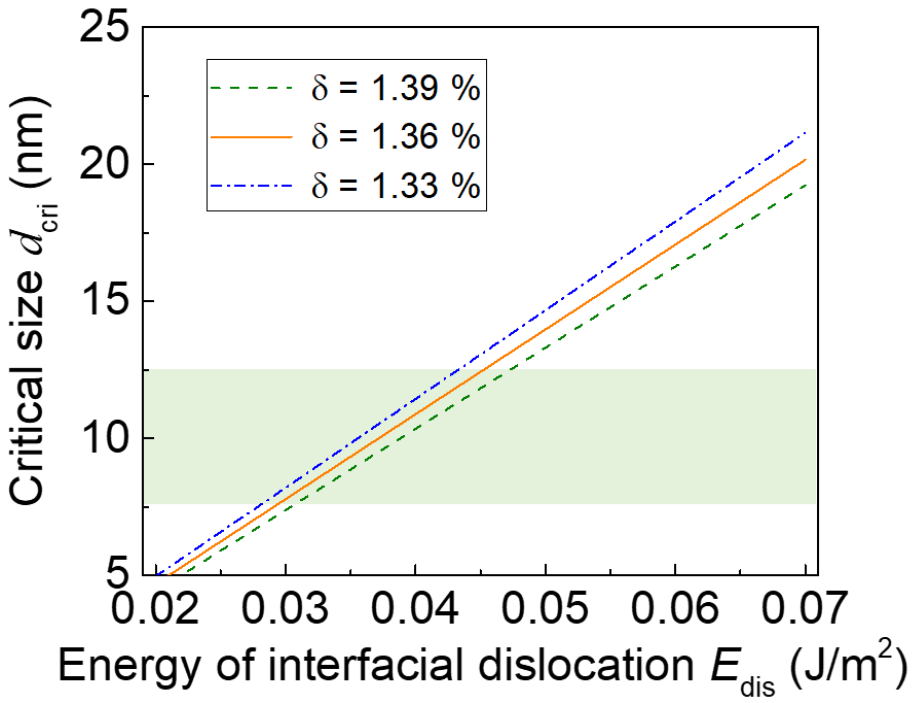

Supplementary Figure 7 | Calculations on the critical size for Al_3Sc particle losing coherency. Theoretical prediction of the critical size (d_{cri}), above which the Al_3Sc nanoprecipitate loss its interfacial coherency. The prediction is based on an equilibrium elastic energy model[S15] that leads to the expression as $d_{cri} = \frac{3 \cdot E_{dis}\,(1-\nu)}{G\,\delta^2(1+\nu)}$, where E_{dis} is the energy of interfacial dislocation network per unit area (~ 0.03 – 0.05 J/m^2 for Al_3Sc nanoprecipitate[S12]), G (≈ 28.0 GPa) and ν (≈ 1/3) is the shear modulus and Poisson ratio of the matrix[S13], respectively; δ is the lattice misfit between the Al_3Sc and the matrix, which, theoretically evaluated to be 1.36%[S16], will be slightly changed by the Mg segregation-induced local composition variation at Al_3Sc/matrix interface.

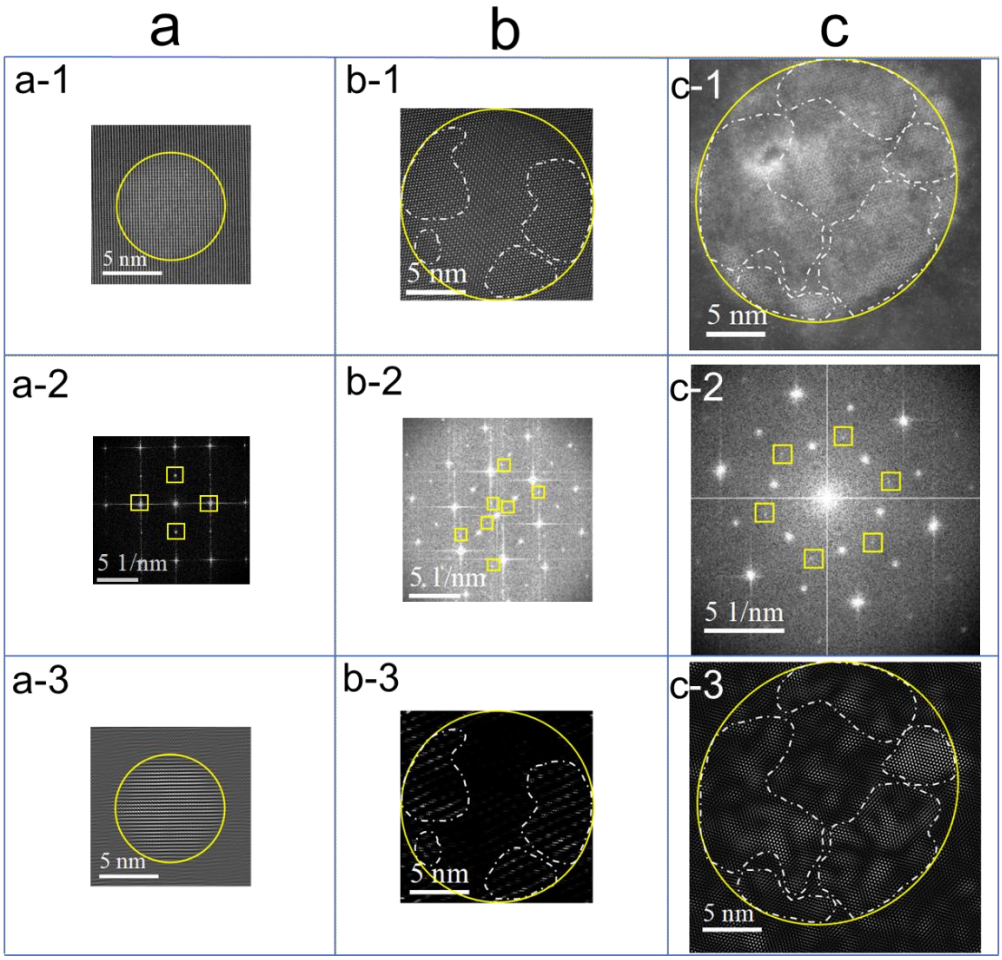

Supplementary Figure 8 | Size effect of the in-situ phase transformation. Representative HAADF-STEM images (top row), corresponding FFT images (middle raw), and IFT images (bottom raw) to index the Al_3Sc phase in (a), and the $Al_3(Mg,Sc)_2$ phase in (b,c) showing its distribution upon Al_3Sc nanoprecipitates in different sizes. This figure corresponds to the sketch in Fig. 2e. In 1 and 3, the yellow sold lines outline the nanoprecipitates, while the white dash lines locates the $Al_3(Mg,Sc)_2$ phases. (a), (b) and (c) correspond to nanoprecipitate with a size of ~ 9, ~ 15, and ~ 28 nm, respectively. The IFT images are based on the diffraction spots marked in FFT images correspondingly.

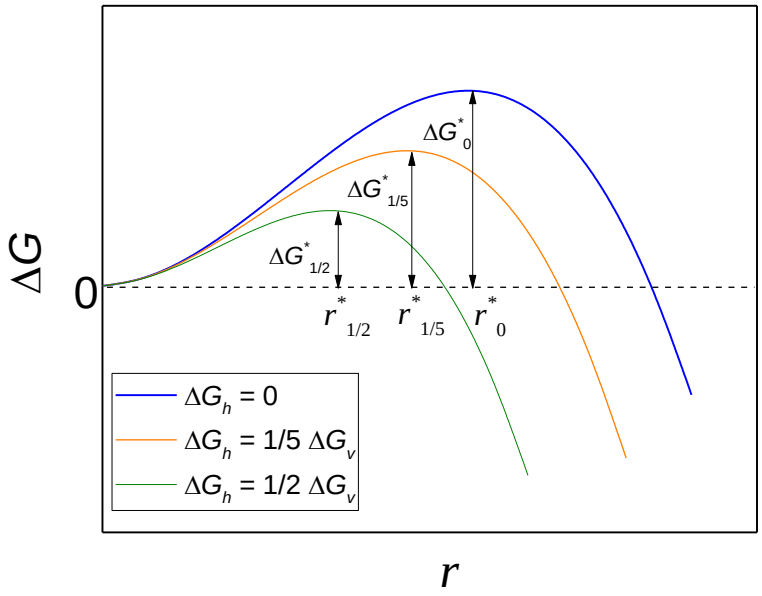

Supplementary Figure 9 | Heterogeneous nucleation of the in-situ phase transformation. The variation of ΔG with r for a homogeneous and heterogeneous nucleus for comparison. The activation energy barrier ΔG^*(corresponding to the critical size r^*) decreases in the heterogeneous nucleation. $\Delta G_h = 0$ represents a homogeneous nucleation.

Supplementary Note 1 | Theoretical basis for the heterogeneous nucleation. According to the solid-state phase transformation theory, the nucleation of a new phase causes a change in the total free energy (ΔG) that can be expressed as follows[S17]:

$$\Delta G = -V \cdot \Delta G_v + A \cdot \gamma + V \cdot \Delta G_s, \qquad \text{(S-1)}$$

where V and A are the volume fraction and interface area of the nucleating embryo, respectively; γ is the interfacial energy; ΔG_v represents the driving force for the transformation per unit volume, and ΔG_s the misfit strain energy per unit volume. Without loss of generality, the embryo is assumed to be a sphere that have a radius of r. Eq. (S-1) is rewritten as

$$\Delta G = -\frac{4}{3}\pi r^3 \cdot (\Delta G_v - \Delta G_s) + 4\pi r^2 \cdot \gamma. \qquad \text{(S-2)}$$

Defining $\Delta G_V = \Delta G_v - \Delta G_s$, the critical embryo size (r^*) and the critical nucleation energy (ΔG^*) can be determined from the differentiation of Eq. (S-2):

$$r^* = \frac{2\gamma}{\Delta G_V}, \qquad \Delta G^* = \frac{16\pi \cdot \gamma^3}{3 \cdot \Delta G_V^2}. \qquad \text{(S-3)}$$

The above critical parameters are applicable to homogenous nucleation, which are termed r_0^*

and ΔG_0^*, respectively. The complex metallic phase Al_3Mg_2 generally nucleates at grain boundaries, as observed in experiments[S18]. This indicates that the homogeneous nucleation of the Al_3Mg_2 phase is quite difficult, additional energy provided by heterogenous sites is preferential for its nucleation. In present work, the Al_3Sc nanoprecipitates formed and dispersed within the grain interior during the first-step heat treatment could serve as potential heterogeneous sites for the Al_3Mg_2 phase nucleation. It is fortunate that the Al_3Mg, a meta-stable precursor to the Al_3Mg_2 phase, share a same $L1_2$ crystal structure with the Al_3Sc and their lattice constants are very close[S19]. This enables the Al_3Mg precursor, heterogeneously nucleated on the Al_3Sc, to gradually evolve into the $Al_3(Mg,Sc)_2$ phase. In this case, the change in the total free energy should consider the additional contribution from the heterogeneous sites (ΔG_{het}):

$$\Delta G = -\frac{4}{3}\pi r^3 \cdot \Delta G_V + 4\pi r^2 \cdot \gamma - \Delta G_{het}. \quad \text{(S-4)}$$

As observed in the present work, the new phase is nucleated at the interfacial dislocations, where the elastic field induced by the interfacial dislocations promotes the nucleation. It is thus reasonable to assume that the ΔG_{het} scales with the volume fraction *V*, *i.e.*, $\Delta G_{het} = V \cdot \Delta G_h$, where ΔG_h is the interfacial dislocation-induced elastic energy per volume. Eq. (S-4) is reduced to:

$$\Delta G = -\frac{4}{3}\pi r^3 \cdot (\Delta G_V + \Delta G_h) + 4\pi r^2 \cdot \gamma. \quad \text{(S-5)}$$

Similarly, r^* and ΔG^* at the heterogeneous nucleation are respectively given by

$$r^* = \frac{2\gamma}{(\Delta G_V + \Delta G_h)}, \qquad \Delta G^* = \frac{16\pi \cdot \gamma^3}{3 \cdot (\Delta G_V + \Delta G_h)^2}. \quad \text{(S-6)}$$

Taking $\Delta G_h = \frac{1}{5}\Delta G_V$ or $\frac{1}{2}\Delta G_V$ for evaluation, the calculations show a significant decrease in both r^* and ΔG^*, see the Supplementary Fig. 9 above. As a smaller r^* and a smaller ΔG^* means an easier nucleation, these results manifest the preferential $Al_3(Mg,Sc)_2$ nucleation/formation heterogeneously on the Al_3Sc nanoprecipitates.

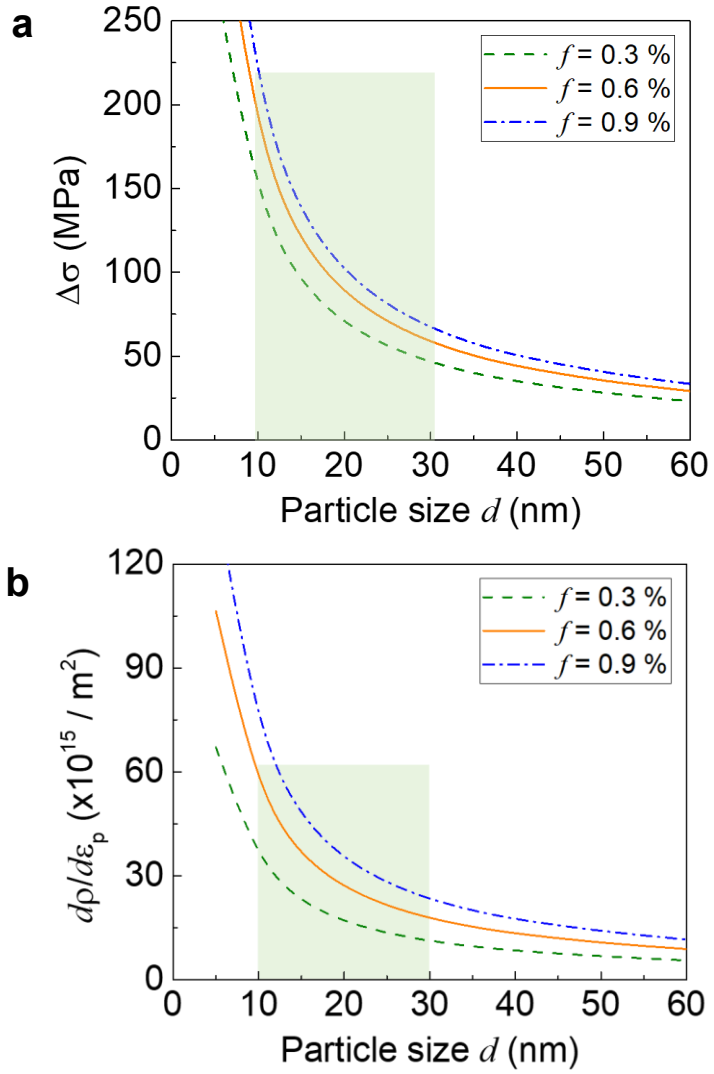

Supplementary Figure 10 | Calculations on the precipitate strengthening and strain hardening. (a) Strengthening by nanoprecipitates: the increment in yield strength ($\Delta\sigma$) depending on the particle volume fraction (f) as a function of particle size d, which follows the strengthening model[S20] as $\Delta\sigma = \frac{\varphi\, G\, b}{\lambda} = \frac{\varphi\, G\, b}{d}\left(\frac{6\,f}{\pi}\right)^{1/3}$, with G (≈ 28.0 GPa) and b (= 0.286 nm) being the shear modulus and Burgers vector of the Al matrix [S15], respectively, and φ being a constant close to 1. (b) Strain hardening induced by the Al_3Sc nanoprecipitates can be approximately given [S21] by the incremental rate of stored dislocation density ($\frac{d\rho}{d\varepsilon_p}$) as $\frac{d\rho}{d\varepsilon_p} = \frac{1}{\lambda^2}\frac{dn_\perp}{d\varepsilon_p} = \frac{M\cdot d}{b\cdot\lambda^2} = \frac{M}{b\cdot d}\left(\frac{6\cdot f}{\pi}\right)^{2/3}$, where $\frac{dn_\perp}{d\varepsilon_p}$ represents the rate of dislocations pinned by nanoprecipitates, and M (= 3.1) is the Taylor factor [S15]. It is quantitatively revealed from (a) that the $\Delta\sigma$ contributed by 10 nm nanoparticles is over three times of that by the 30 nm ones.

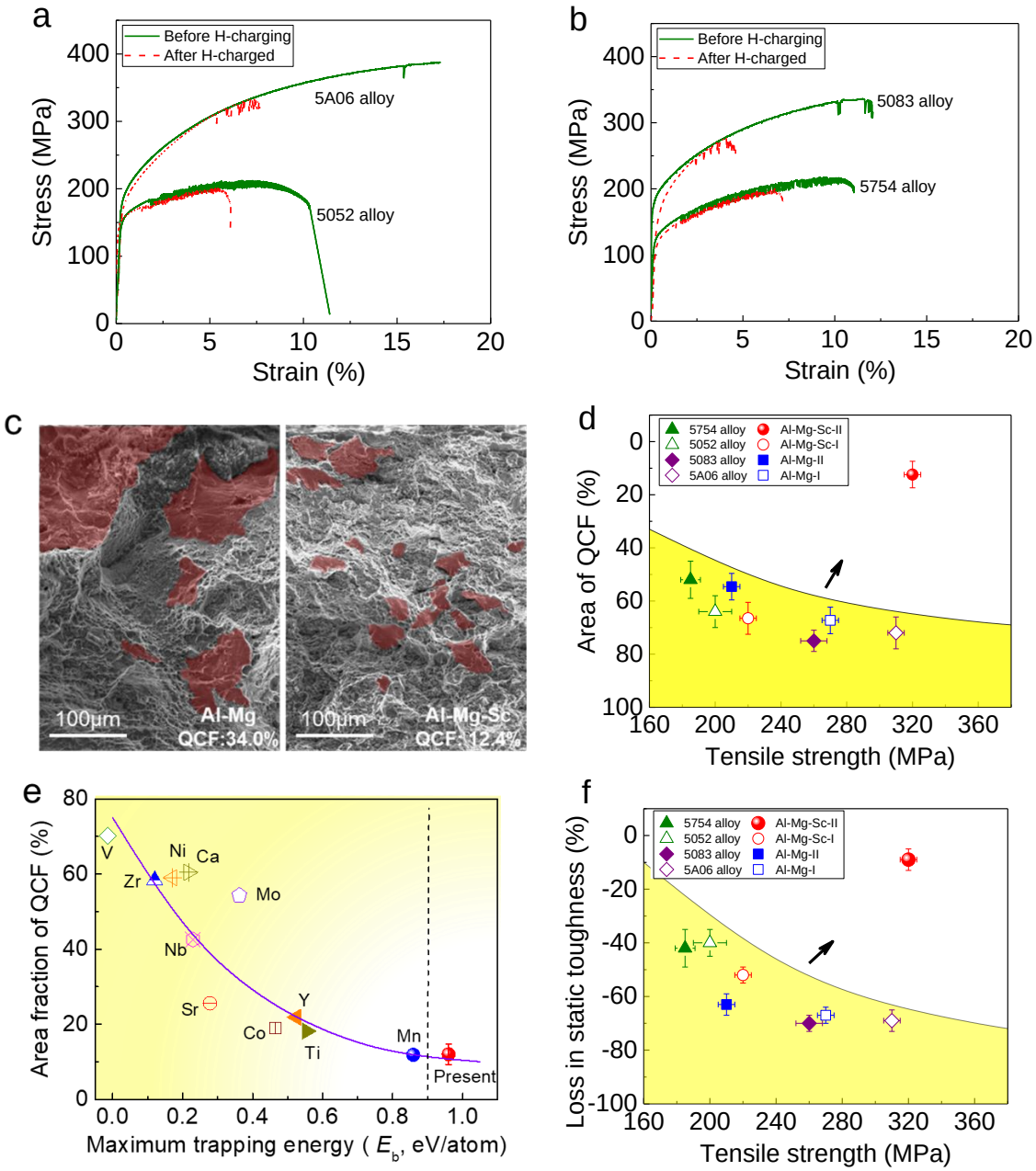

Supplementary Figure 11 | More tensile results for comparison. Representative tensile stress-strain curves of commercial 5xxx alloys before and after ~7.0 ppmw H-charging: (a) 5A06 and 5052 alloys, and (b) 5083 and 5754 alloys. Representative fracture surface SEM images showing the percentage of QCF (highlighted by red color) of H-charged Al-Mg-II and Al-Mg-Sc-II alloys for comparison. (d) Experimental results on the area of QCF vs. tensile strength of the studied eight Al-Mg-based alloys for comparison. (e) Summary of the area fraction of QCF varied with the maximum H-trapping energy in Al alloys containing different ICPs [S1,S22-S24] in comparison with present Al-Mg-Sc-II alloy. (f) Loss in static toughness vs. tensile strength of the studied alloys for comparison. The static toughness is calculated from S-S curves by $U = \int_0^{\varepsilon_f} \sigma \, d\varepsilon$ where σ is the flow stress and ε_f is the strain at fracture. The error bars of present data are the standard deviation of the mean ($n > 3$).

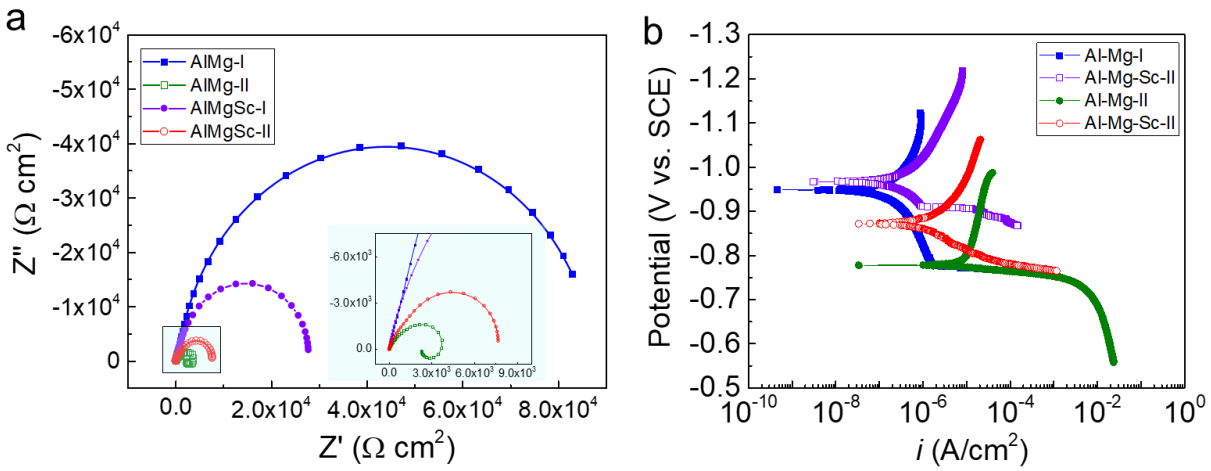

Supplementary Figure 12 | Electrochemical properties of the alloys for comparison. (a) Electrochemical impedance spectra (Nyquist curves) and (b) polarization curves of present four alloys for comparison. It is expected that the Al-Mg-II alloy, with massive precipitation of large Al_3Mg_2 particles at grain boundaries, should show a strong susceptibility to corrosion, which is clearly revealed from above results. In comparison, the Sc addition improves the corrosion resistance of Al-Mg-Sc-II. Note that both the Al-Mg-I and Al-Mg-II alloys, although showing a corrosion resistance seemingly superior to Al-Mg-Sc-II, will suffer from a sensitization effect (forming intergranular Al_3Mg_2 precipitates) at relatively low temperatures in service. The Al-Mg-Sc-II alloy will be highly stable, because it has experienced the second-step heat treatment and the Samson-$Al_3(Mg,Sc)_2$ phase has been uniformly precipitated within the grain interior.

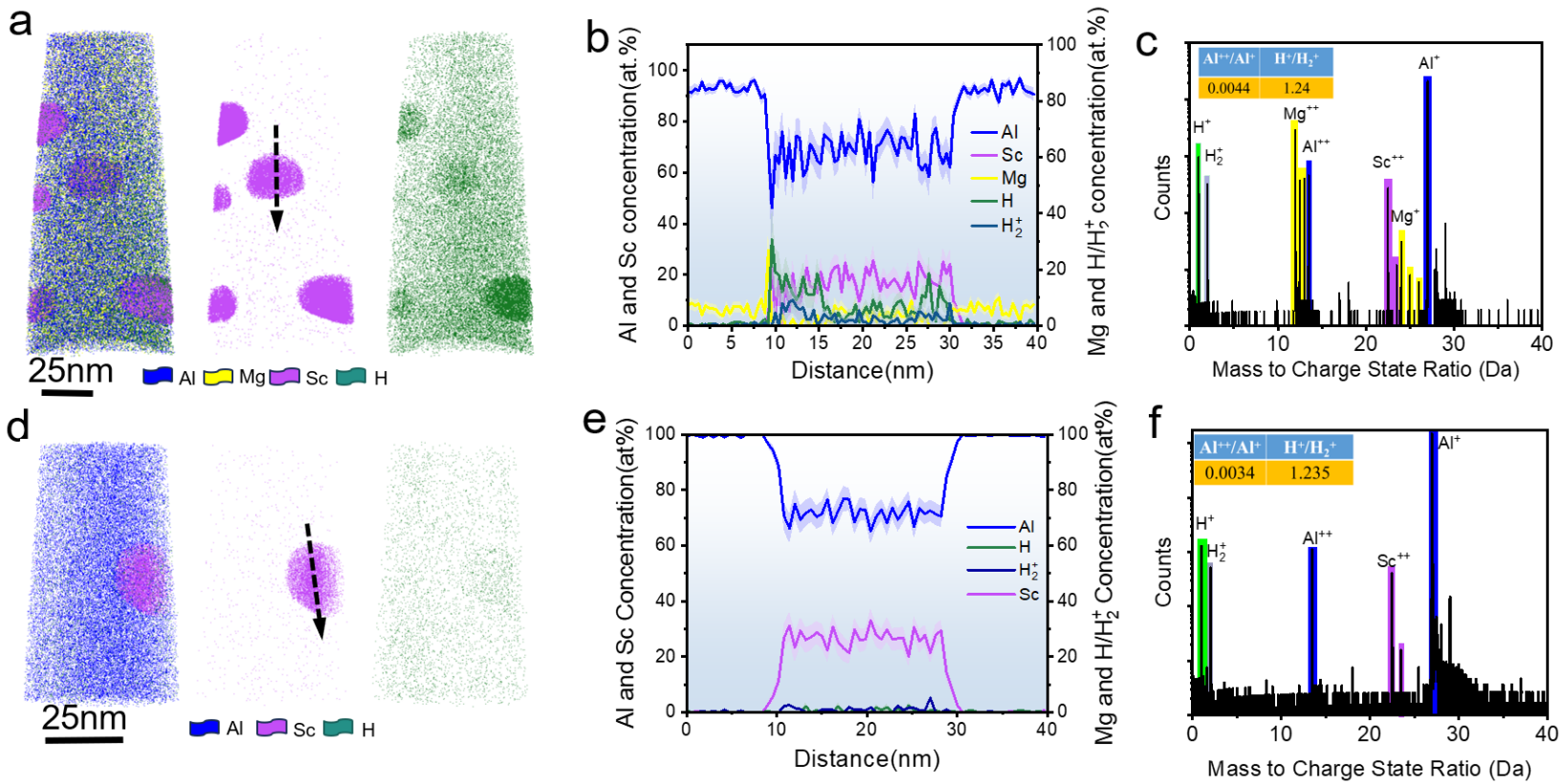

Supplementary Figure 13 | APT examinations under laser pulsing mode. (a) APT reconstruction images to show the coupled nanoprecipitates and H distribution in electropolished Al-Mg-Sc-II alloy. (b) 1D profile element concentration distributions cross a nanoprecipitate as indicated in (a). A high H concentration is evidenced at the outer layer of the nanoprecipitate, which corresponds to the $Al_3(Mg, Sc)_2$ nanophase. (c) Relevant mass spectrum for APT analysis. The shaded bands of the traces correspond to the standard deviations of the counting statistics in each bin of the profile. (d)-(f) are corresponding results for Al_3Sc nanoprecipitates in electropolished Al-Sc-II alloy. A much low H concentration is found that means a week H-trapping capability in the Al_3Sc nanoprecipitates. Standard error is shown in (b) and (e), respectively.

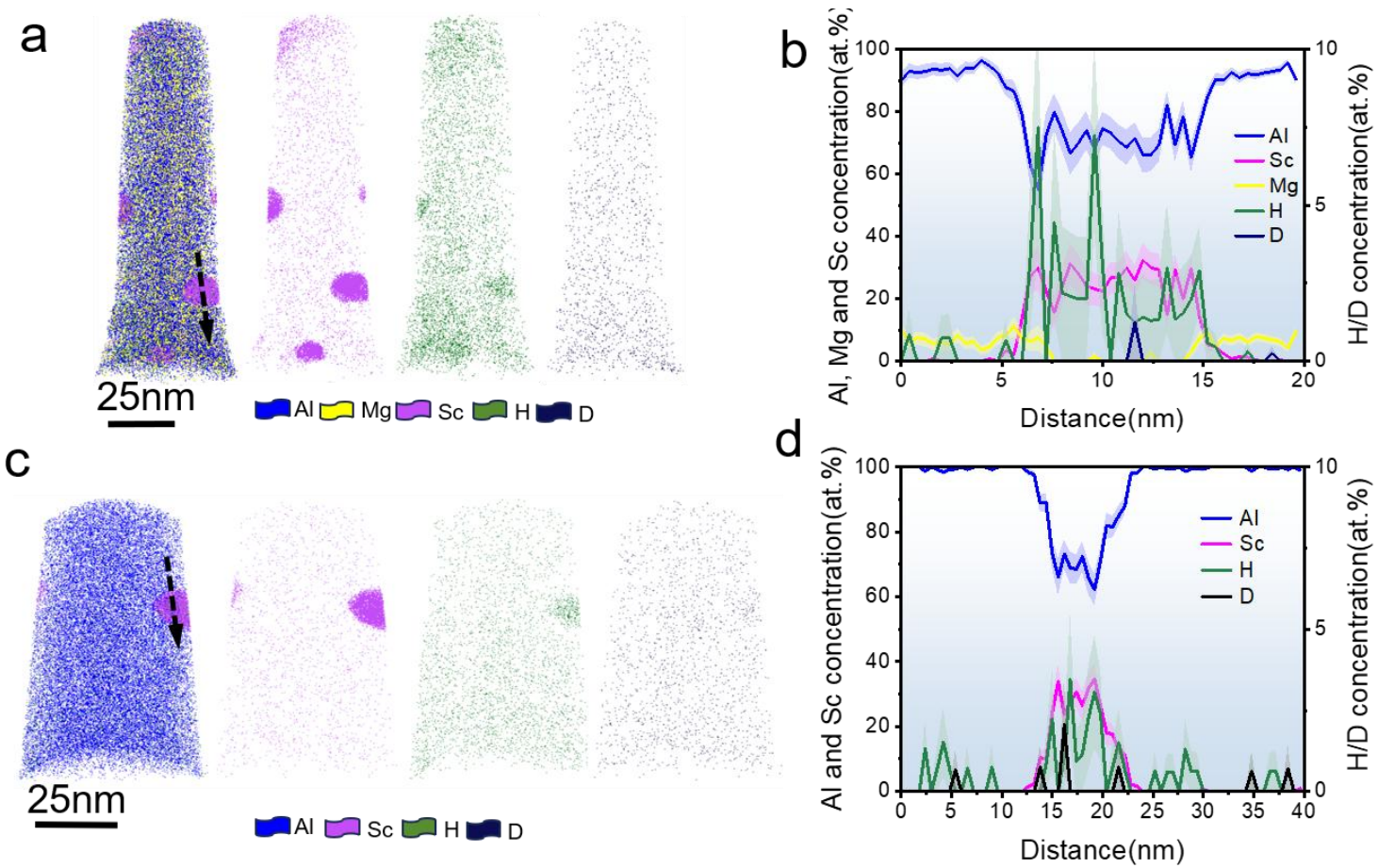

Supplementary Figure 14 | Cryo-APT examinations under HV pulsing mode. (a) APT reconstruction images to show the coupled nanoprecipitates and H distribution in H-charged Al-Mg-Sc-II alloy. (b) 1D profile element concentration distributions cross a nanoprecipitate as indicated in (a). A high H concentration is detected at the nanoprecipitate. (c) and (d) are corresponding results for Al_3Sc nanoprecipitates in H-charged Al-Sc-II alloy. A low H concentration is obvious that means a week H-trapping capability in the Al_3Sc nanoprecipitates. Standard error is shown in (b) and (d), respectively.

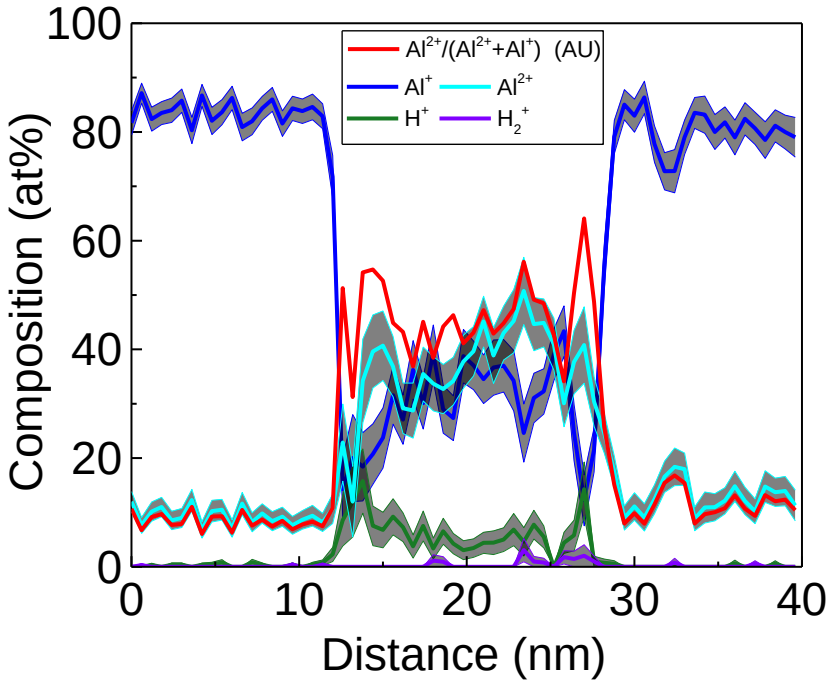

Supplementary Figure 15 | High H-trapping at $Al_3(Mg,Sc)_2$ shell revealed by APT. Relative composition of H^+, H_2^+, Al^+ and Al^{2+} measured across the nanoprecipitate/matrix interface in the Al-Mg-Sc-II alloy examined by APT in HV pulsing mode. The variations in the Al charge-state ratio is also plotted (in red). The electric field is clearly higher in nanoprecipitate, with an increase in the absolute amount of Al^{2+} as well as in the ratio between Al^{2+} and (Al^{2+} + Al^+). Based on the reports by Kellogg [S21], a higher field should result in a lower amount of H originating from the residual gas. Therefore, the detected background H in matrix should be lower than in the nanoprecipitate, and with values measured of up to > 20 at.%, the H in nanoprecipitate must be mostly from solute hydrogen. Standard error is shown in this figure.

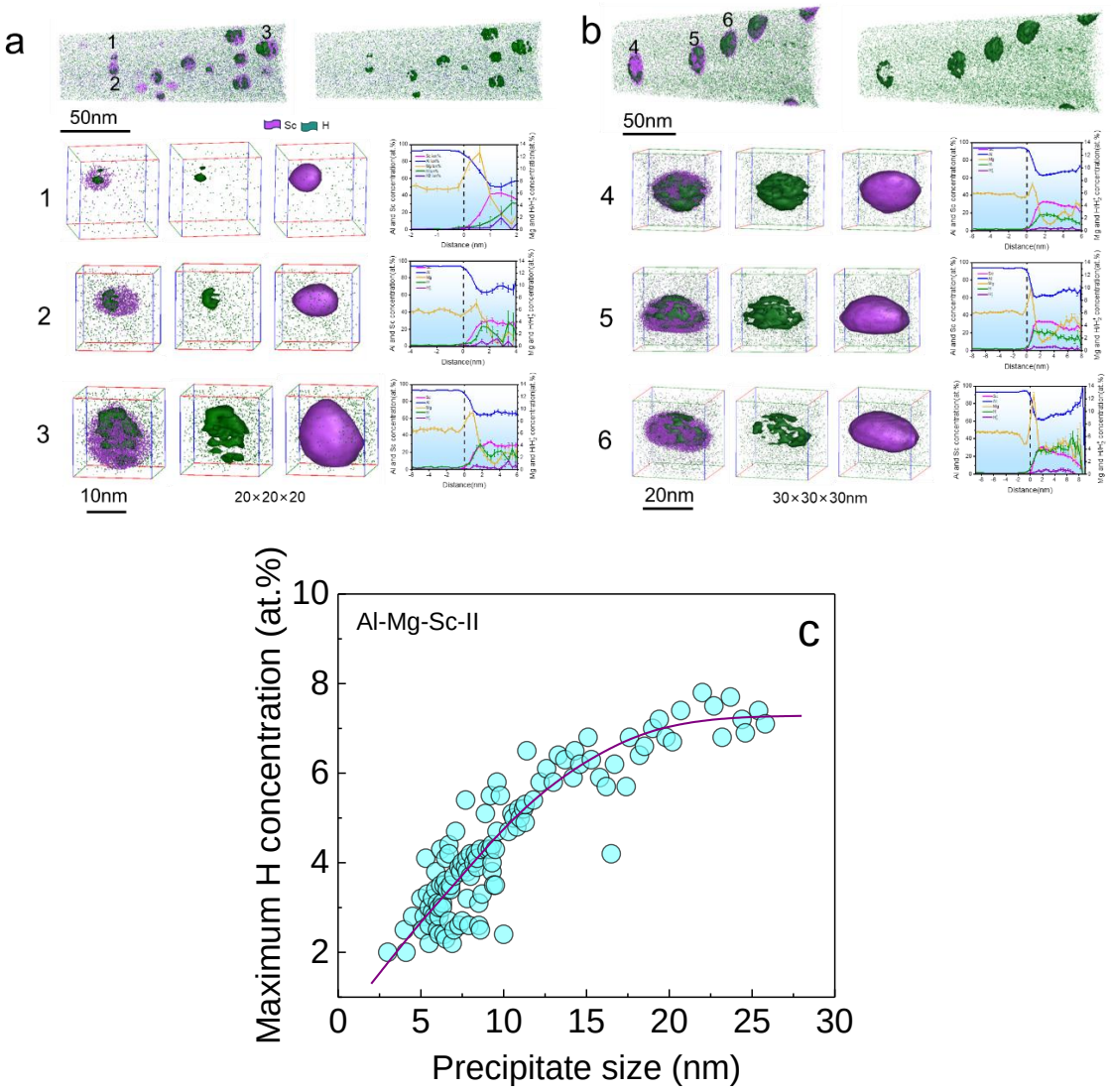

Supplementary Figure 16 | Particle size-dependent H-trapping determined by APT. Representative APT images to show H trapped at nanoprecipitates with different sizes in the electropolished Al-Mg-Sc-II alloy. Particles numbered 1, 2, and 3 in (a) and 4, 5, and 6 in (b) represent different sizes for direct comparison. Iso-composition surface of 3.0 at.% H and 3.0 at.% Sc is respectively presented in the figures. (c) Statistical results on the maximum H concentration at nanoprecipitates with different sizes, measured from the APT proxigram. The sold line is a guide to the eyes.

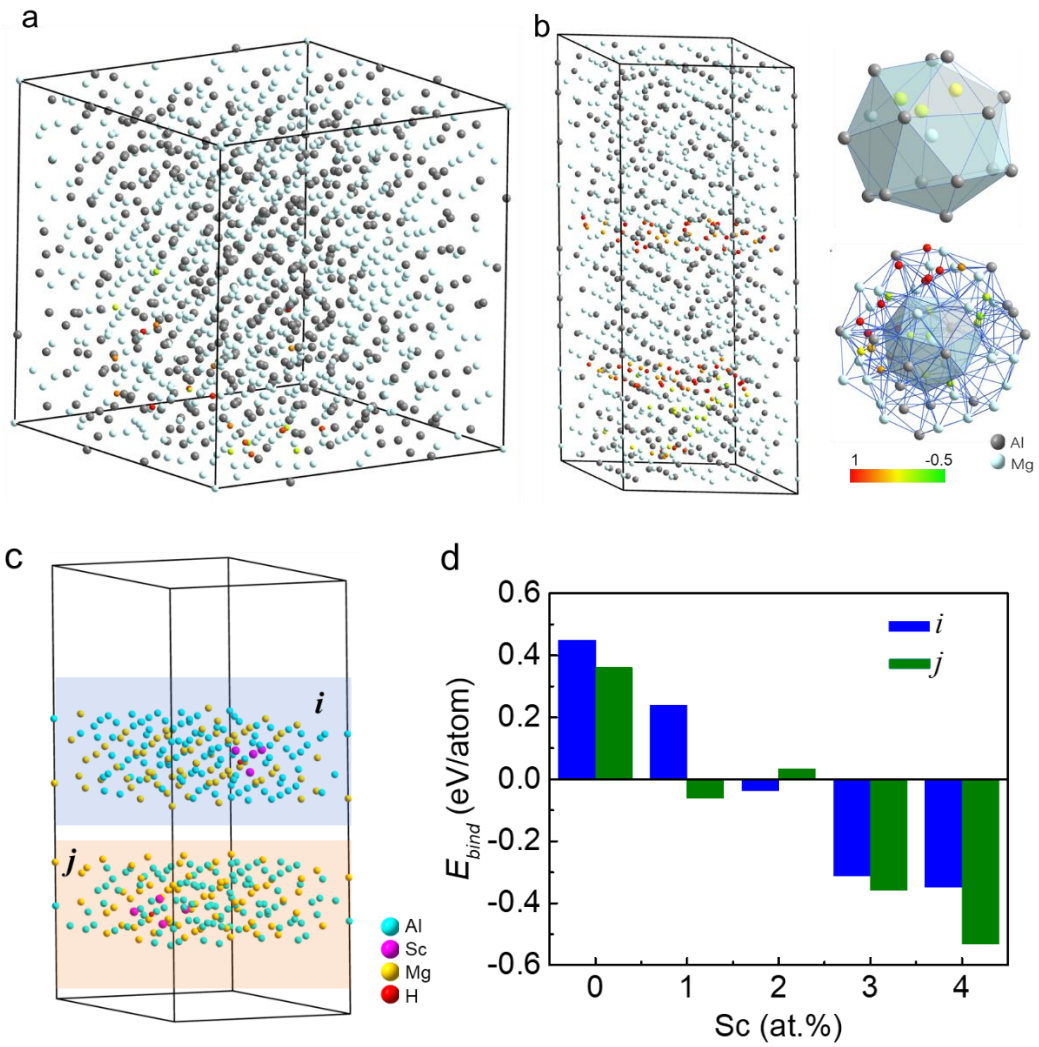

Supplementary Figure 17 | Simulations on the H-trapping energy. (a) C-model: the cubic β-Al_3Mg_2 phase used for calculation of H-trapping energy, where some H atoms are placed in typical sites for illustration. (b) R-model: the rhombohedral β′-Al_3Mg_2 phase used for calculations, with some H atoms (red or yellow for different trapping energy) placed in typical trapping site of the structure. A1-type nanocluster is shown for visualization (right part): top is the inner shell and bottom the two shells. Red or yellow dots in the structures represent H atoms with different trapping energy (see text for more description). (c, d) DFT simulation results show the Sc atoms partially occupying Mg atoms in the β′-Al_3Mg_2 phase results in a stronger binding with H, indicative of a higher H-trapping energy. (c) is the slab model for simulation, where two typical layers (*i* and *j*) were used. Some H atoms are placed in typical trapping sites for example. (d) Binding energy with H, E_{bind}, gradually reduces as the Sc atoms increasing.

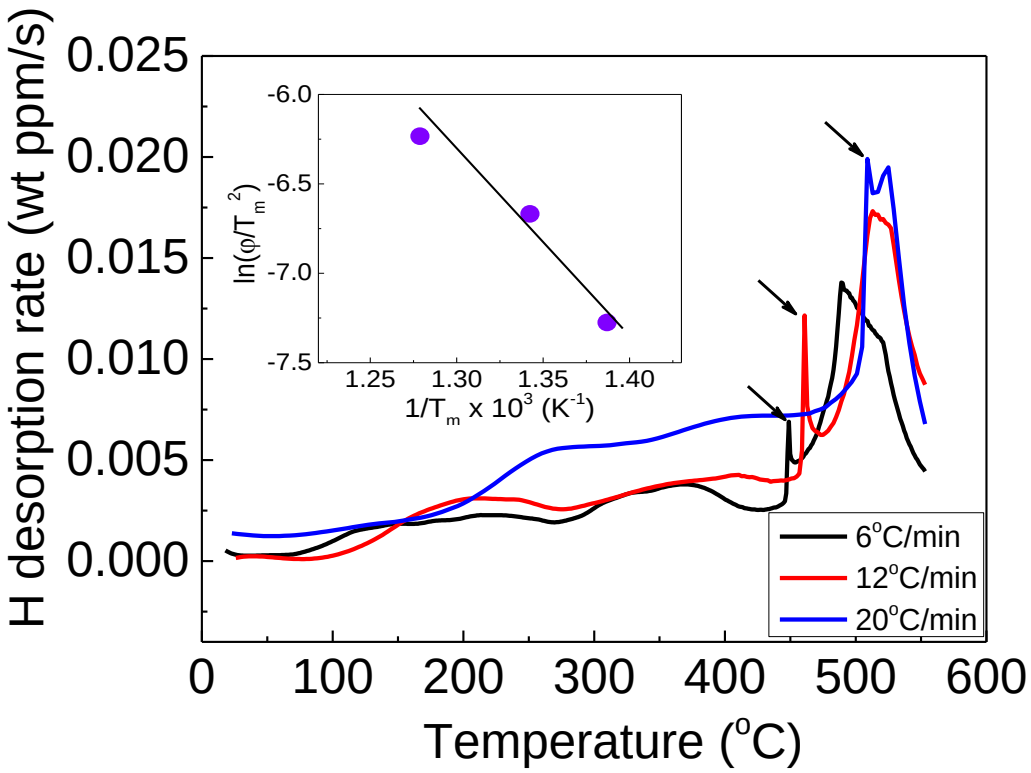

Supplementary Figure 18 | TDS measurements on the H-trapping energy. Hydrogen desorption spectra of the Al-Mg-Sc-II alloy at different heating rates. The peaks associated with the $Al_3(Mg,Sc)_2$ phase are indicated by arrows. Insert is the corresponding energy calculation by Choo-Lee method[S25]. The TDS results yield a H-binding energy of $E_b \sim 81.4 \pm 3.6$ kJ/mol (equal to ~ 0.85 eV/atom), close to the DFT results of ~ 0.90 eV/atom.

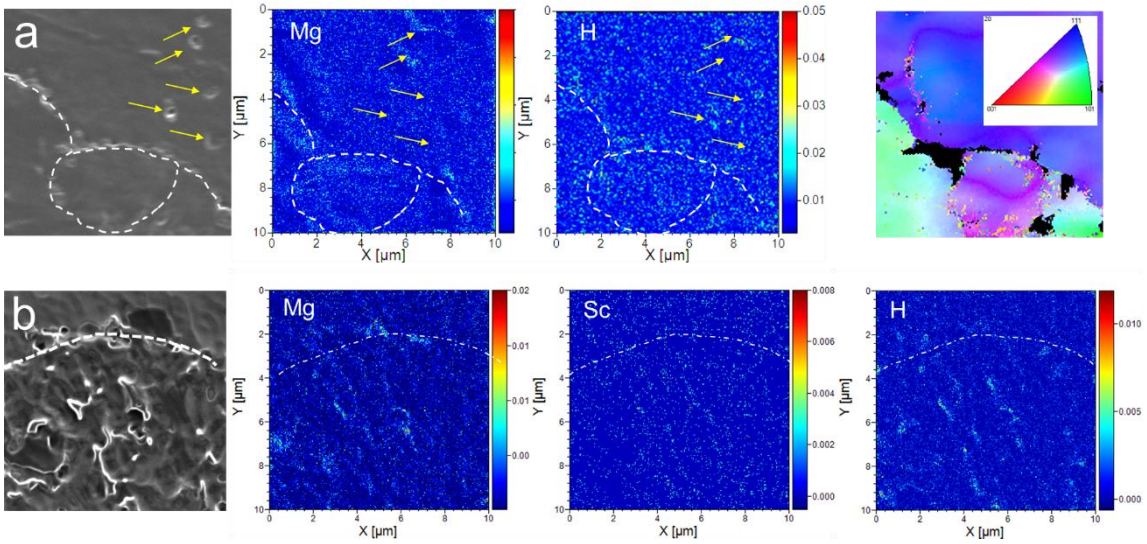

Supplementary Figure 19 | ToF-SIMS results to show H-trapping behavior. Representative ToF-SIMS images of the H-charged Al-Mg-II (a) and Al-Mg-Sc-II (b) alloys for comparison. The examination area is 10 × 10 µm for both figures. A large particle precipitated at grain boundary is detected in the Al-Mg-II alloy, shown as black region in the EBSD image (a). Dash lines in the figures represent grain boundaries. In the Al-Mg-II, a high concentration of Mg and H are measured at and near grain boundaries, a combination previously showed to favor embrittlement. In the Al-Mg-Sc-II, Mg, Sc and H are found co-located within the grain interior, indicative H trapped by the intragranular distribution of Mg-Sc-containing precipitates, with no obvious Mg or H enrichment at the grain boundaries. These results support the claims that Mg is mainly precipitated within the grain interior in the Al-Mg-Sc-II alloy that traps more H and suppresses the intergranular H segregation.

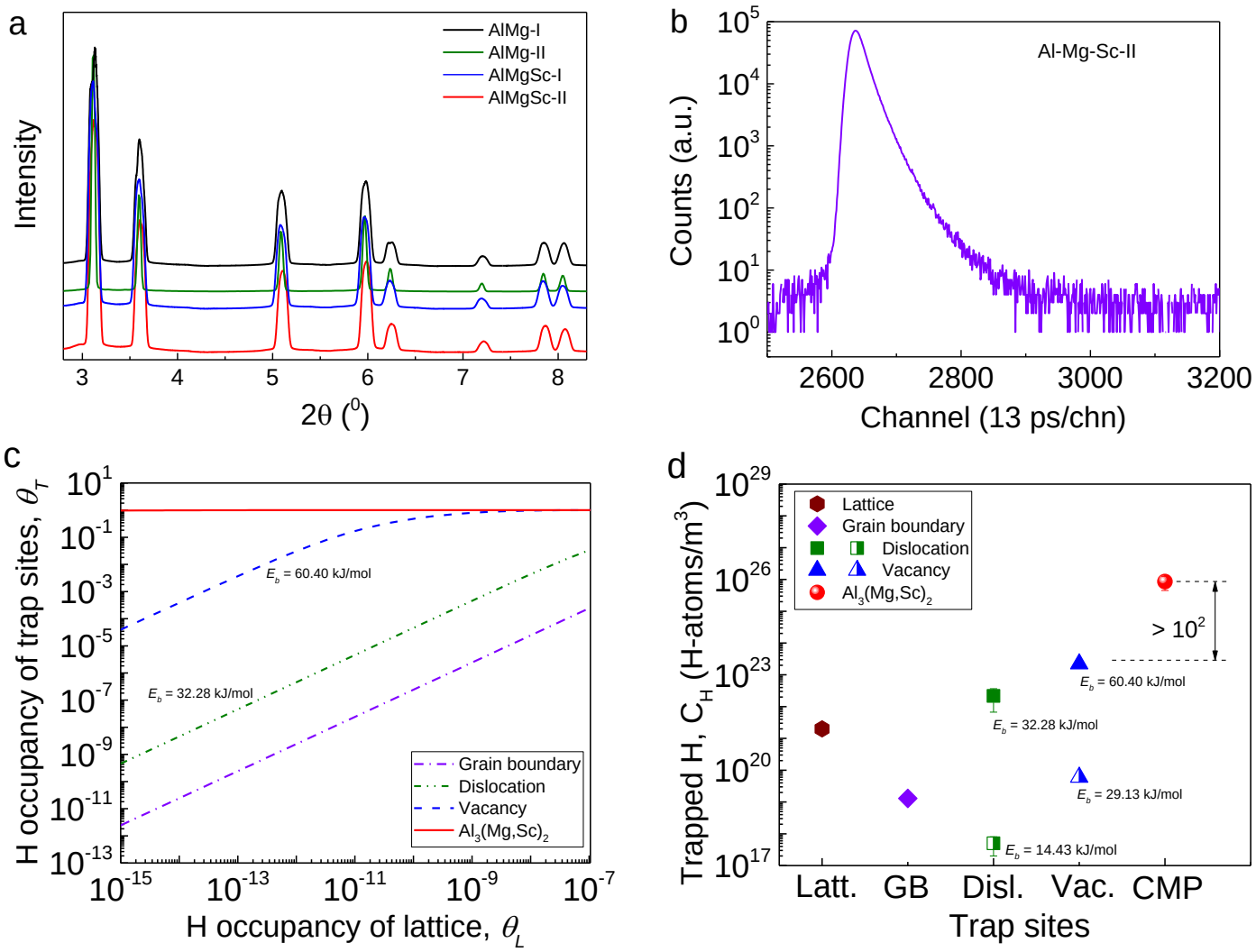

Supplementary Figure 20 | H-trapping contributed by different microstructural features. (a) Synchrotron X-ray diffraction pattern of the four alloys studied in present work. (b) Positron annihilation lifetime spectrum of the Al-Mg-Sc-II alloy. Calculations results: (c) the hydrogen occupancy of different trap sites depending on the H occupancy of lattice; (d) Trapped H concentration at different sites in the Al-Mg-Sc-II alloy. Different E_d of dislocation and vacancy are evaluated for comparison in (d).

Supplementary Note 2 | Evaluation of the H-trapping by different microstructural features. According to the thermal equilibrium theory [S26], H trapped at different site is in equilibrium with that at normal lattice sites. The H occupancy in each trap sites is thus calculated as [S27]:

$$\frac{\theta_i}{1-\theta_i} = \theta_L \exp\left(\frac{E_{b,i}}{RT}\right), \quad \text{(S-7)}$$

where $E_{b,i}$ is the trap binding energy, R is the gas constant (8.31 J·mol^{-1}·K^{-1}), T is the absolute temperature, and θ_L and θ_i are the occupancies of lattice sites and other trap sites (i = grain boundaries, dislocations, vacancies, and nanoprecipitates), respectively. The total hydrogen concentration, C_H^T, is expressed as the sum of the hydrogen concentration at all trap sites as follows [S27,S28]:

$$C_H^T = \theta_L N_L + \sum \theta_i N_i, \quad \text{(S-8)}$$

where N_L and N_i are the trap site densities in the interstitial lattice site and the i^{th} trap site in atoms per unit volume, respectively. Note that the pore contribution is not considered here, because the alloys were prepared by using twin-roll casting, where the rolling effect during cast will eliminate the micropores as much as possible. In addition, the four alloys studied in this work contain micropores approximately in the same number density, size, and volume fraction. This indicates that the micropores should be not the predominant factor that causes a significant difference in HE resistance between the Al-Mg-Sc-II alloy with the other three alloys.

The determination of trap site density for grain boundaries is based on an assumption of equiaxed grains. The trap site density for dislocations, vacancies, and nanoprecipitates is respectively evaluated in terms of their parameters, such as number density, volume fraction, and concentration. The hydrogen trap interval is corresponding to the maximum density at which hydrogen can present in each trap site, *i.e.*, trapped hydrogen content when the occupancy is equal to 1. These are 22 atomH/nm^2 for the grain boundaries [S29], 2.8 atomH/nm for the edge dislocation [S30], 8 atomH/vacancy for the vacancies [S31], and 10 atomH/nm^3 for present nanoprecipitates. Using the experimentally measured parameters (see Supplementary Table-3) in combination with the reported H-binding energy (E_b, as given in Supplementary Table-4), the H occupancy and trapped H concentration at different sites can be assessed. Note that there are differences in the reported E_b, especially of dislocation [S32,S33] and vacancy [S31,S33], different E_b taken from references (see Supplementary Table-4) are considered for comparison.

For the Al-Mg-Sc-II alloy, Supplementary Fig. 19c shows the H occupancy of grain boundaries, dislocations, vacancies, and $Al_3(Mg, Sc)_2$ nanoprecipitates depending on the H occupancy of lattice. It is clearly revealed that the H occupancy of nanoprecipitates is much greater than other trap sites, and almost keeps a constant of 1 over the wide θ_L range from 10^{-15} to 10^{-7}. This means that the nanoprecipitates trap the H strongly. Supplementary Fig. 19d compares the H concentration trapped at different sites. The H trapped at nanoprecipitates is 2 to 7 orders of magnitude greater than at other sites, indicative of a predominant H accumulation.

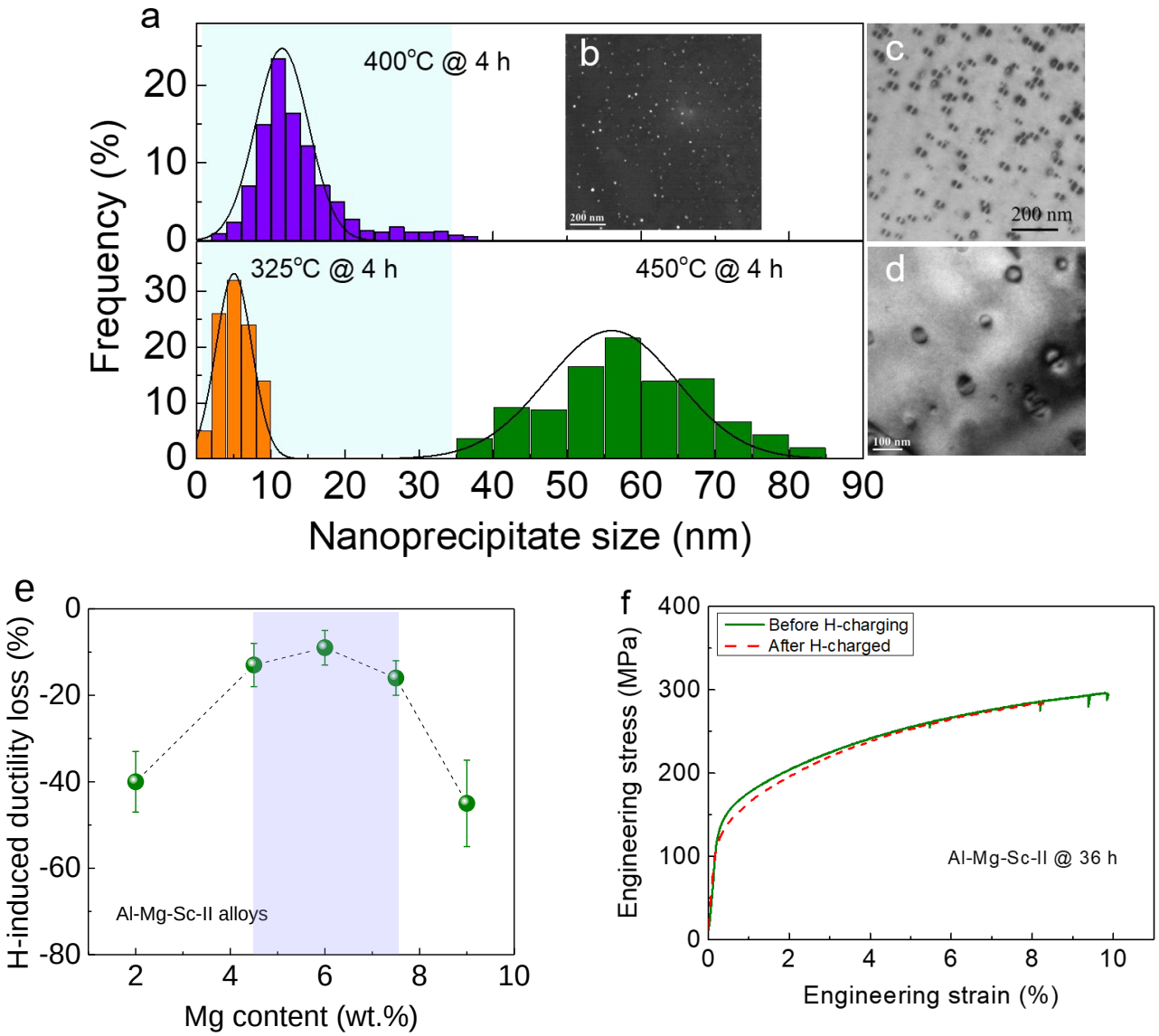

Supplementary Figure 21 | Processing and composition windows for the present H-tolerance. and (a) Size distribution of Al_3Sc nanoprecipitates in the Al-Mg-Sc-I alloy aged at 400 °C for 4 h (top), 325 °C for 4 h (bottom left), and 450 °C for 4 h (bottom right). The cyan background represents the optimal size range that covers dual-sized regimes. Only the 400 °C-aged alloy matches the optimal size range. (b) is a representative dark-field TEM image of the 400 °C-aged alloy, and (c) and (d) are bright-field TEM images of the 325 °C- and 450 °C-aged alloy, respectively. (e) The effect of Mg content on the H-induced tensile elongation loss. The shadow region represents effective Mg content for present phenomenon. All the alloys are charged by ~ 7 ppmw. (f) Representative S-S curves of the 36 h-treated Al-Mg-Sc-II alloys before H-charging (solid line) and after H-charged (dash line), for comparison. The tensile elongation is reduced by ~20 % after H-charging. The error bars in (e) are the standard deviation of the mean ($n > 3$).

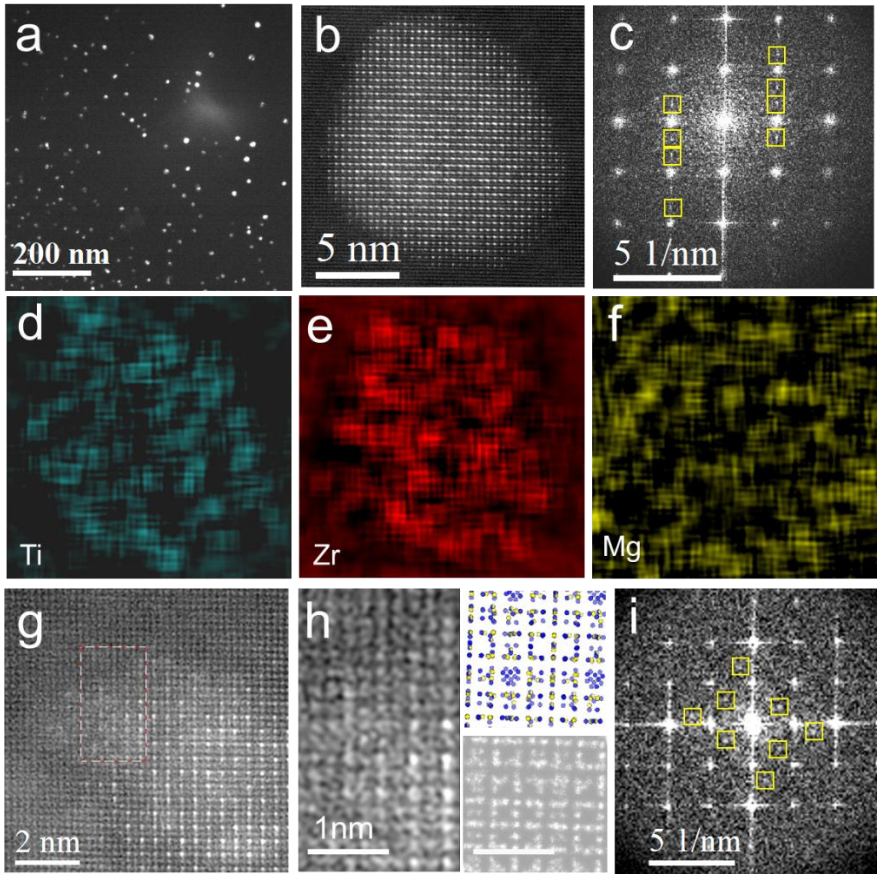

Supplementary Figure 22 | The present design strategy applied in Al-Mg-Zr-Ti alloy. (a) A representative low-magnification TEM image to show a high-density dispersion of nanoprecipitates created in a twin-roll cast Al-6.0 wt.%Mg-0.34wt.% Zr-0.18wt.% Ti alloy (Al-Mg-Zr-Ti-II alloy, with Zr and Ti replacing Sc). A representative HAADF-STEM image (b) and corresponding FFT image (c) to identify the Al_3Mg_2 phase at the nanoprecipitate. Zr, Ti, and Mg elemental atomic mapping (d-f, respectively) corresponding to the nanoprecipitate in (b). A typical HAADF-STEM image (g) indicates the Al_3Mg_2 phase formed on a Al_3(Ti,Zr) nanoprecipitate (bottle right part), as marked by a rectangle. (h) Zoom-in image corresponding to the square region in g, in comparison with the simulation image and crystal structure sketch. The Al_3Mg_2 phase is indexed by FFT image as shown in (i). The zone axis is $[\bar{1}\bar{3}4\bar{1}]_{\beta'}$.

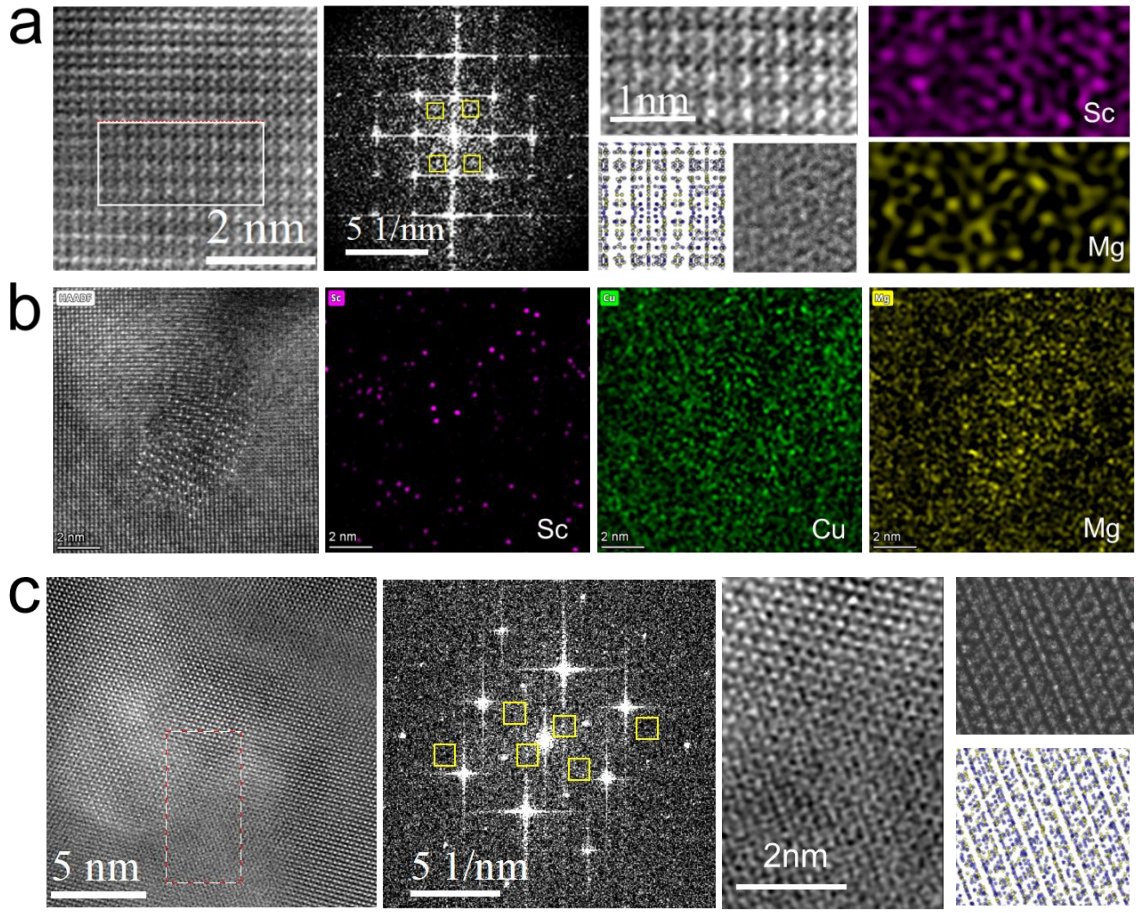

Supplementary Figure 23 | The present design strategy applied in other Al alloys. (a) A representative HAADF-STEM image to show the Al_3Mg_2 phase on a Al_3Sc nanoprecipitate in a twin-roll cast Al-6.0 wt.%Mg-1.0 wt.% Cu-0.3 wt.% Sc alloy (Al-Mg-Cu-Sc-II alloy, with Cu addition to increase the strength), with FFT image, zoom-in image in comparison with the simulation results and crystal structure sketch, and Mg and Sc elemental atomic mapping corresponding to the marked region. (b) A representative HAADF-STEM image to show a *S'*-Al_2CuMg nanoprecipitate in the Al-Mg-Cu-Sc-II alloy with corresponding Sc, Cu, and Mg elemental atomic mapping, respectively. (c) A representative HAADF-STEM image and corresponding FFT image to show the Al_3Mg_2 phase on a Al_3Sc nanoprecipitate in a twin-roll cast Al-6.0 wt.% Mg-1.0 wt.% Zn-0.3 wt.% Sc alloy (Al-Mg-Zn-Sc-II alloy, with Zn addition to improve the mechanical properties), together with zoom-in image in comparison with the simulation results and crystal structure sketch corresponding to the region marked in the left.

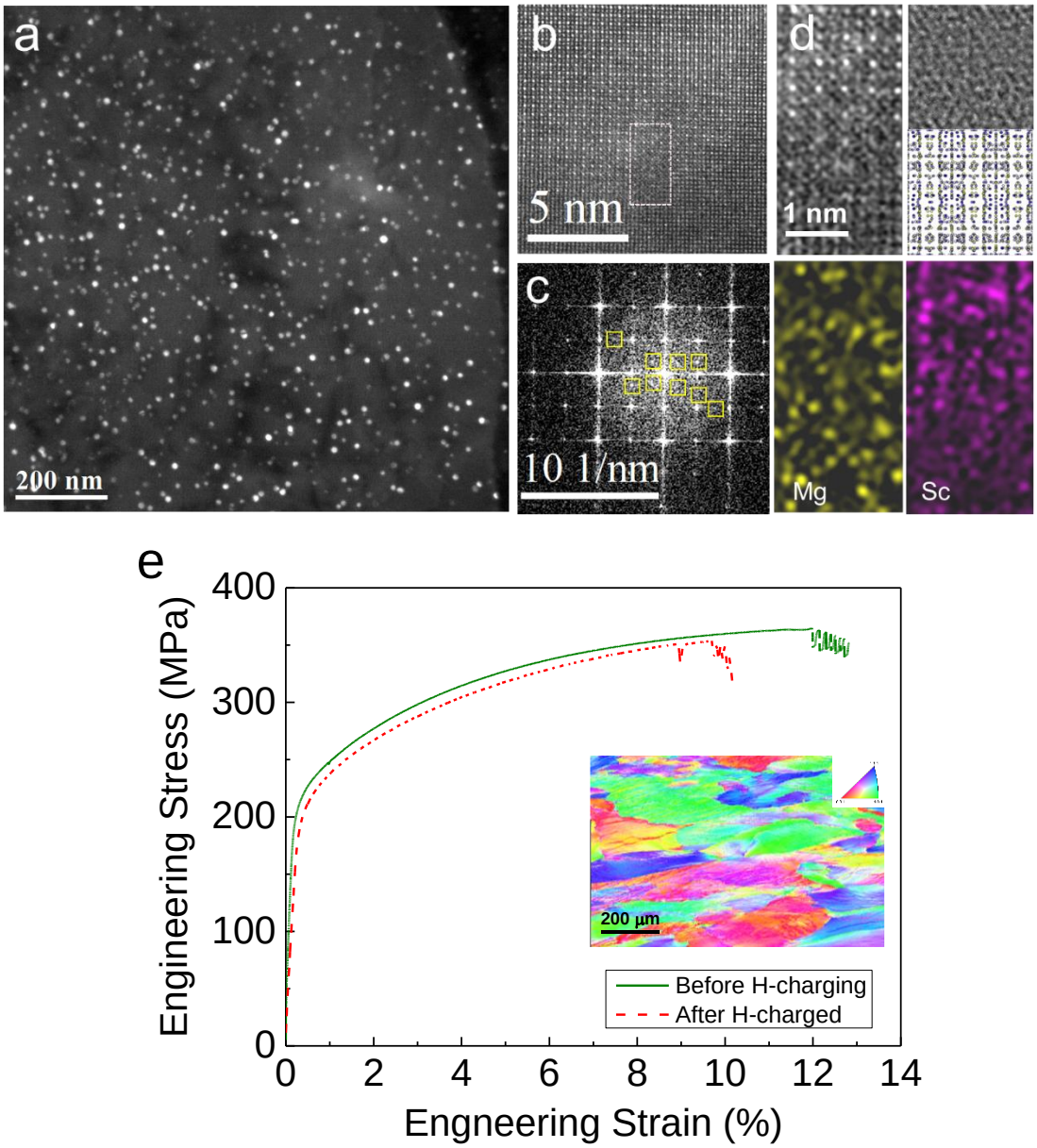

Supplementary Figure 24 | Scale-up of present Al-Mg-Sc-II alloy. (a) A representative low-magnification TEM image to show a high-density dispersion of nanoprecipitates in the scale-up Al-Mg-Sc-II alloy. A representative HAADF-STEM image (a) and corresponding FFT image (c) to show the $Al_3(Mg,Sc)_2$ phase formation on a Al_3Sc nanoprecipitate. (d) A zoom-in image corresponding to the region marked by rectangle in (b), in comparison with simulation results and crystal structure sketch. Corresponding Mg and Sc elemental atomic mappings are also presented in (d). (e) Representative stress-strain curves of the scale-up Al-Mg-Sc-II alloy before and after ~7 ppmw H-charged. Insert in (e) is a representative EBSD image showing the grains of the scale-up alloy.

Supplementary Table 1 | Peaks indexed in Supplementary Fig. 4i

2 theta	(hkl)
2.83	β (8 8 0)
2.87	β' (8 $\bar{4}$ $\bar{4}$ 0)
2.95	β' (7 $\bar{4}$ $\bar{3}$ 11)
3.04	β' ($\bar{7}$ 7 0 7)
3.19	β (12 4 2)
3.30	β' ($\bar{8}$ 7 1 6)
3.33	β' ($\bar{8}$ 7 1 9)

Supplementary Table 2 | Peaks indexed in Fig. 1k

2 theta	(hkl)
2.83	β (8 8 0)
2.87	β' (8 $\bar{4}$ $\bar{4}$ 0)
2.95	β' (7 $\bar{4}$ $\bar{3}$ 11)
3.19	β (12 4 2)
3.30	β' ($\bar{8}$ 7 1 6)
4.71	β (18 4 4)
4.77	β' (11 $\bar{7}$ $\bar{4}$ 18)

Supplementary Table 3 | Experimental results of the microstructural features

Alloys	Grain size (μm)	Dislocation density (m^{-2})	Vacancy concentration (%)
Al-Mg-Sc-II	106 ± 23	$(7.75\pm0.35)\times10^{13}$	$(5.87\pm0.33)\times10^{-4}$
Al-Mg-II	230 ± 42	$(4.82\pm0.42)\times10^{13}$	-
Al-Mg-Sc-I	96 ± 27	$(1.12\pm0.24)\times10^{14}$	-
Al-Mg-I	211 ± 35	$(8.91\pm0.67)\times10^{13}$	-

Supplementary Table 4 | Summary of hydrogen binding energy of different trap sites

Trap site	Grain boundary	Dislocation		Vacancy	
E_b (kJ/mol)	19.30	14.43	32.28	29.13	60.40
Reference	[S28]	[S32]	[S33]	[S31]	[S33]

Supplementary references

S1. Xu, Y. T., Toda, H., Shimizu, K., *et al.* Suppressed hydrogen embrittlement of high-strength Al alloys by Mn-rich intermetallic compound particles. *Acta Mater.* **236**, 118110 (2022).

S2. Wang, Y. F., Sharma, B., Xu, Y. T., *et al.* Switching nanoprecipitates to resist hydrogen embrittlement in high-strength aluminum alloys. *Nature Comm.* **13**, 6860 (2022).

S3. Sun, Y. W., *et al*. Localized corrosion behavior associated with Al_7Cu_2Fe intermetallic in Al-Zn-Mg-Cu-Zr alloy. *J. Alloys Comp.* **783**, 329-340 (2019).

S4. Kimura, T., *et al*. Combined factors for enhanced high-temperature strength of Al-Mn-Cr heat-resistant alloy fabricated using laser-based powder bed fusion. *Mater. Charact.* **196**, 112618 (2023).

S5. Kang, H. J., *et al*. 3-D morphology and growth mechanism of primary Al_6Mn intermetallic compound in directionally solidified Al-3 at.% Mn alloy. *Intermetallics* **23**, 32-38 (2012).

S6. Lee, I. S., *et al*. Formation of Al-Mo intermetallic particle-strengthened aluminum alloys by friction stir processing. *Intermetallics* **35**, 9-14 (2013).

S7. Flament, C., *et al*. Stability of β″ nano-phases in Al-Mg-Si(-Cu) alloy under high dose ion irradiation. *Acta Mater.* **128**, 64-76 (2017).

S8. Deschamps, A., *et al*. Influence of pre-deformation on ageing in an Al-Zn-Mg alloys. I: Microstructure evolution and mechanical properties. *Acta Mater.* **47**, 281-292 (1999).

S9. Radmilovici, V., *et al*. Structure and morphology of S-phase precipitates in Aluminum. *Acta Mater.* **47**, 3987-3997 (1999).

S10. Guo, Z. Y., Zhao, G. & Chen, X. G. Effects of two-step homogenization on precipitation behavior of Al_3Zr dispersoids and recrystallization resistance in 7150 aluminum alloy. *Mater. Charact.* **102**, 122-130 (2015).

S11. Mondolfo, L.F. Aluminum Alloys: Structure and Properties, *Butterworths* (1976).

S12. Iwamura, S. & Miura, Y. Loss in coherency and coarsening behavior of Al_3Sc precipitates. *Acta Mater.* **52**, 591-600 (2004).

S13. Liu, G. et al. Modeling the strengthening response to aging process of heat-treatable aluminum alloys containing plate/disc or rod/needle-shaped precipitates. *Mater. Sci. Eng. A* **344**, 113–124 (2003).

S14. Blatov, V. A., Llyushin, G. D. & Proserplo, D. M. Nanocluster model of intermetallic

compounds with giant unit cells: β, β′-Mg_2Al_3 polymorphs. *Inorg. Chem.* **49**, 1811-1818 (2010).

S15. Wasser, W. A. Misfit accommodation by imperfect dislocations in epitaxial fcc films. *J. Appl. Phys.* **41**, 39-41 (1970).

S16. Røyset, J. & Ryum, N. Scandium in aluminium alloys. *Inter. Mater. Rev.* **50**, 19-44 (2005).

S17. Porter, D. A., Easterling, K. E. & Sherif, M. Y. Phase Transformations in Metals and Alloys. CRC Press (2021).

S18. McMahon, M. E., *et al.* Beta phase distribution in Al-Mg alloys of varying composition and temper. *Corro. Sci.* **169**, 108618 (2020).

S19. Osamura, K. & Ogura, T. Metastable phases in the early stage of precipitation in Al-Mg alloys. *Metall. Trans. A* **15**, 835-842 (1984).

S20. Miller W. S. & Humphreys F. J. Strengthening Mechanisms in Particulate Metal Matrix Composites. *Scripta Mater.* **25**, 33-38 (1991).

S21. Liu, G., Zhang, G. J., Jiang, F., *et al*. Nanostructured high-strength molybdenum alloys with unprecedented tensile ductility. *Nature Mater.* **14**, 344-350 (2013).

S22. Sun, B. H., *et al*. Chemical heterogeneity enhances hydrogen resistance in high-strength steels. *Nature Mater.* **20**, 1629-1634 (2021).

S23. Safyari, M., Moshtaghi, M., Kuramoto, S. On the role of traps in the microstructural control of environmental hydrogen embrittlement of a 7xxx series aluminum alloy. *J. Alloy Compd*. **855**, 157300 (2021).

S24. Su, H., *et al.* Influence of hydrogen on strain localization and fracture behavior in Al-Zn-Mg-Cu aluminum alloys. *Acta Mater*. **159**, 332-343 (2018).

S25. Choo, W. Y. & Lee, J. Y. Thermal-analysis of trapped hydrogen in pure iron. *Metall. Trans. A* **13**, 135-140 (1982).

S26. Oriani, R. A. The diffusion and trapping of hydrogen in steels. *Acta Metall.* **18**, 147-157 (1970).

S27. Oriani, R. & Josephic, P. Equilibrium and kinetic studies of the hydrogen-assisted cracking of steel. *Acta Metall.* **25**, 979–988 (1977).

S28. Smith, S.W. & Scully J. R. The identification of hydrogen trapping states in an Al-Li-Cu-Zr alloy using thermal desorption spectroscopy. *Metall. Mater. Trans. A* **31**, 179-193 (2000).

S29. Yamaguchi, M., Ebihara, K, I., Itakura, M., *et al.* First-principles calculation of

multiple hydrogen segregation along aluminum grain boundaries. *Compu. Mater. Sci.* **156**, 368-75 (2019).

S30. Shimizu, K., *et al*. Hydrogen partitioning behavior and related hydrogen embrittlement in Al-Zn-Mg alloys. *Eng. Frac. Mech.* **216**, 106503 (2019).

S31. Ismer, L., Park, M. S., Janotti, A., *et al*. Interactions between hydrogen impurities and vacancies in Mg and Al: A comparative analysis based on density functional theory. *Phys. Rev. B* **81**, 184110 (2010).

S32 Yamaguchi, M., *et al*. Hydrogen-trapping energy in screw and edge dislocations in aluminum: First-principles calculations. *Mater. Trans.* **62**, 582-589 (2021).

S33. Safyari, M., Khossossi, N., Meisel, T., *et al*. New insight into hydrogen trapping and embrittlement in high strength aluminum alloys. *Corro. Sci.* **223**, 111453 (2023).